Site Selective Spectroscopy of CaF_2:Eu^{3+} Nanoparticles

A THESIS
SUBMITTED IN PARTIAL FULFILMENT
OF THE REQUIREMENTS FOR THE DEGREE OF
MASTER OF SCIENCE IN PHYSICS
AT THE
UNIVERSITY OF CANTERBURY

by

Adam J. Pamplin

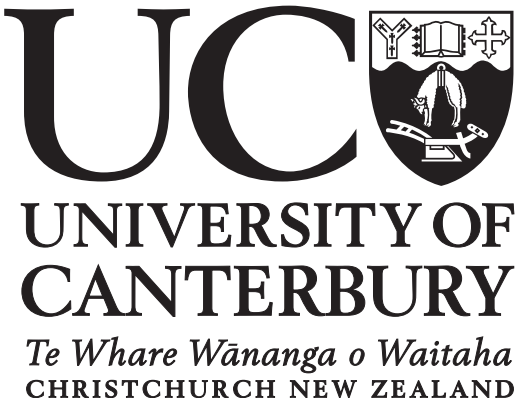

2017

Site Selective Spectroscopy of CaF_2:Eu^{3+} Nanoparticles

Adam J. Pamplin

M.Sc. Thesis 2017
Supervisors: Professor Mike Reid & Professor Jon-Paul Wells

Abstract

Trivalent europium doped calcium fluoride nanoparticles have been investigated using laser site selective spectroscopy. In these core only particles, four distinct spectroscopic centres have been observed, using excitation into the $^5D_0$ and $^5D_1$ multiplets of Eu^{3+}. The sites labelled 1/1a display very similar spectroscopic properties including an absence of emission from the $^5D_1$ multiplet. It is suggested that these centres are two related configurations of quite low symmetry, residing on or near the surface of the nanoparticle. Two further sites, labelled sites 2/2a exhibit much longer lifetimes and $^5D_1$ emission is observed. We tentatively conclude that these are centres embedded within the nanoparticle. Site 2 shares spectroscopic features with the $C_{2v}(Na^+)$ centres observed in bulk co-doped samples whilst site 2a appears to exhibit 17.4 ms $^5D_0$ lifetimes which is closely similar to cubic centres in the bulk crystals.

Acknowledgements

I would like to acknowledge and thank my supervisors Professors Jon-Paul Wells and Mike Reid for their guidance and support in this thesis.

Thanks also go out to Graeme MacDonald for his assistance with electronics and with helping me interface them appropriately for the experiment, Orlon Petterson for helping me arrange the software required for data collection, and both Stephen Hemmingsen and Wayne Smith for their technical assistance, particularly keeping my laser fuelled with nitrogen gas. I'd also like to give fellow postgraduate student Alex Neiman thanks for his advice when first getting acquainted with experimental work and equipment.

I would also like to thank the Department of Physics & Astronomy at UC for assisting with living costs through the year with a scholarship, as well as a position as a Senior Lab Demonstrator and Teaching Assistant within the department.

Finally, thanks and acknowledgements go to my fellow postgraduate students, particularly Jonty Scott and Ben Roberts for their camaraderie and humour during this long year.

Contents

List of Figures

List of Tables

Chapter 1

Introduction

Rare-earth (specifically lanthanide) doped substances have many applications in areas ranging from fluorescent lighting to lasing materials, as well as medical imaging and telecommunications. These applications arise due to the unique optical properties of the rare-earths, as well as a very high quantum efficiency and durability [1]. By placing rare-earth ions into a crystal, experimentation allows insight into the quantum mechanical behaviour of these rare-earth ions in different symmetry sites of the crystal.

Due to advancement of nanocrystal synthesis methods, lanthanide-doped nanoparticles (NPs) have become more available for research in the field of bioimaging. Inorganic materials such as nanoprobes used in this context are well sought after, due to their unique electromagnetic and optical properties. Lanthanide-doped nanoparticles have three main applications in bioimaging. These are downshifting luminescence (DSL), upconversion (UC), and magnetic resonance (MR). These methods offer unique ways of observing the morphology of a tissue and as a result, have great potential for noninvasive visualisation.

In this study, excitation and fluorescence spectroscopy were performed on sodium stabilised calcium fluoride nanocrystals, doped with a modest concentration of trivalent europium ions (CaF_2:Eu^{3+}). Fluorescence lifetimes of the excited multiplets were also measured. These spectra were then compared to analogous spectra of the bulk crystals collected in previous studies with crystals grown by the vertical Bridgman-Stockbarger technique.

1.1 Motivation

Trivalent rare-earth ions have unique optical properties due to an effect called the lanthanide contraction. This rises as a result of a shielded valence shell and the result of this shielding, is a contracted $4f$ radial wavefunction. Due to this wavefunction having a probability density inside the filled $5p$ and $5s$ shells, there is minimal interaction with the ion's environment (ie. a host crystal lattice) and this leads to transitions between different electronic states being very narrow in frequency. For example, the $^7F_0 \rightarrow {}^5D_0$ transition of the trivalent europium ion is extremely sharp in bulk crystalline hosts [2]. As a consequence of their small interaction with the local environment, the lifetimes of these excited states are also longer than that of other ions (such as transition metals) used in condensed matter optical applications.

Due to the large number of states associated with the $4f$ state, lanthanides are prime

candidates for laser materials. This was first demonstrated in 1960 with the CaF_2:Sm^{2+} laser operating at a temperature of 77 K (liquid nitrogen temperature) [3]. The transition on which this laser operates is at 708.4 nm, which is a strong electric dipole allowed $4f^{N-1}5d \rightarrow 4f^N$ transition. As this transition is allowed by the electric-dipole operator, the strength of the transition is relatively high, compared to a $4f^N \rightarrow 4f^N$ transition; for which electric-dipole transitions are nominally forbidden. Following this application of lanthanides to laser materials, lanthanide nanoparticles may have an interesting application to dye laser systems. It has previously been shown that dye-doped silica nanoparticles can be used as a gain medium to produce a tunable laser [4]. The advantage of a smaller-scale gain medium offers can give rise to increased gain efficiencies in lasing equipment.

Lanthanide doped (dielectric crystal) nanoparticles are interesting to investigate because the small size of these particles can influence their quantum mechanical properties. In addition, ions residing on or near the surface of the nanoparticle can become important. Similar effects have been observed previously for Eu^{3+} doped CaF_2/CdF_2 superlattices. The layers of doped CaF_2 which bordered the CdF_2 were shown to have shifted Eu^{3+} emission, as opposed to ions within the inner layers [5], showing that effective surface sites affect the transitions energies in an easily detectable way spectroscopically. Due to its much larger surface area to volume ratio, the nanoparticles may exhibit surface states, which will emit differently to that of the mostly non-surface dopants in the bulk crystal.

The earliest synthesis of CaF_2:Eu^{3+} nanoparticles (known to the author) was performed by F. Wang et al. in 2004, which utilised a single-step solution-fluorination approach with $CaCl_2$, $EuCl_3$, and NH_4F being used as reactants [6], resulting in spherical nanoparticles with diameters in the range of 15-20 nm. X-ray diffraction was performed on these nanoparticles, along with excitation and fluorescence spectroscopy at room temperature. These types of nanocrystals have also been gamma irradiated, where it was shown to convert Eu^{3+} ions in the nanocrystalline structure to Eu^{2+} [7]. Europium-doped CaF_2 nanocrystals have also been studied in glass-ceramics with respect to annealing time, where the longer annealing time is shown to give rise to a more crystalline structure controlled luminescence from the nanocrystals [8]. No low temperature, high resolution spectroscopy has been performed on europium-doped CaF_2 nanocrystals, to the knowledge of the author.

With the advancement in synthesis of lanthanide-doped nanoparticles, manipulation of crystal phases, sizes, and morphologies can be achieved. Great control over the surface functional groups, which are groups of atoms/molecules on the surface that are responsible for the chemical reactions of the resultant material, can be achieved. The nanoparticles used in this study are CaF_2:Eu^{3+} nanoparticles. Similar nanoparticles with other lanthanide ions have been grown via this method [9]. By developing new techniques to synthesise materials with nanometre dimensions, this presents opportunities to explore properties of these host materials for lanthanide ion doping [10].

Micro-crystals have also been studied, where reaction conditions were shown to affect the morphology and size of the resultant microcrystals [11]. Room temperature spectroscopy was performed, exhibiting very broad spectra. Much like their nanoparticle counterparts, these microcrystals have also been studied inside of transparent glass ceramics, where the structure was studied using X-ray diffraction [12].

The lifetimes of metastable states of lanthanide-doped nanoparticles have been shown to be affected immensely by particle size [13]. Europium has been primarily researched in terms of DSL, as a candidate for strong and practical DSL, where nanoparticles have been suggested as good candidates [14]. These have been recommended, due to the crystal host providing a stable environment for the lanthanide dopants. The risk of the toxic ion leaching into the living tissue is minimal [15]. Y_2SO_2:Eu^{3+} particles conjugated with proteins have been shown to bind to latex beads. This was the first demonstration of time-resolved luminescence imaging in lanthanide doped nanoparticles, and was performed in 1990 [16]. Following this, a breakthrough was made, in which YVO_4:Eu^{3+} NPs modified with guanidine (a colourless solid) on the surface to target Na^+ channels. In this study, the NPs were found to be individually detectable and as a result, the distribution of the Na^+ channels were able to be determined. Through the use of time-gated detectors, the background fluorescence from bacteria and laser light was eliminated [17].

1.2 Lanthanide Doped Dielectric Crystals

The lanthanides are a series on the periodic table of elements, characterised by their unfilled $4f$ orbitals. This series ranges from lanthanum to lutetium, with respective atomic numbers of 58 and 71. The $4f$ orbital of lanthanum is unfilled, whereas lutetium has 14 electrons in its $4f$ orbital (full). So as the lanthanide series continues, the electron count in the $4f$ orbital increases by one in each step. Due to the poor shielding of nuclear charge by the $4f$ electrons and the increasing effective nuclear charge as the series increases, the $4f$ shell has a more probable position closer to the nucleus. This means the $4f$ orbital contracts towards the nucleus, causing the orbital to be positioned closer to the nucleus than either the $5d$ or $6s$ orbitals. This is known as lanthanide contraction.

In this study, the dielectric crystal used to host the lanthanide dopant is calcium fluoride (CaF_2). The crystalline structure of CaF_2 is face-centred cubic (FCC), with calcium cations distributed in alternating cages of 8 fluoride ions. CaF_2 has a molecular weight of 78.07 atomic units and a melting point of 1415 °C [18]. The conduction band of CaF_2 is localised towards the Ca^{2+} orbitals, whereas the valence band is localised towards the F^- orbitals. This band gap has been evaluated at 97,590 cm^{-1} [19]. Due to this large band gap, CaF_2 allows a wide range of transmission wavelengths, which ranges from the vacuum ultra violet (130 nm) to the mid infra red (10 μm) [20]. Absorption at wavelengths over 10 μm increases significantly due to phonon absorption, peaking at approximately 37 μm (270 cm^{-1}) [21].

Lanthanide ions replace calcium cations when doped into the crystal. These elements most often enter the crystal as either divalent or trivalent ions. Divalent ions directly replace calcium ions, but trivalent ions require extra charge compensation to maintain the overall charge neutrality of the crystal. The occupation of an empty cage of fluoride ions with an additional fluoride ion satisfies this requirement for charge balance. In terms of electronic transitions, divalent ions' electron transitions go from the $4f^N$ state to both $4f^N$ and $4f^{N-1}5d$ states, whereas the trivalent ion's electron transitions are $4f^N \rightarrow 4f^N$ transitions. Unlike the $4f$ orbitals, the $5d$ orbitals do not contract. This is important in a crystal because the electrons in the $5d$ orbital will interact strongly with the environment, therefore being affected by the vibrations of the host lattice. Due to this interaction, $4f^N$ -

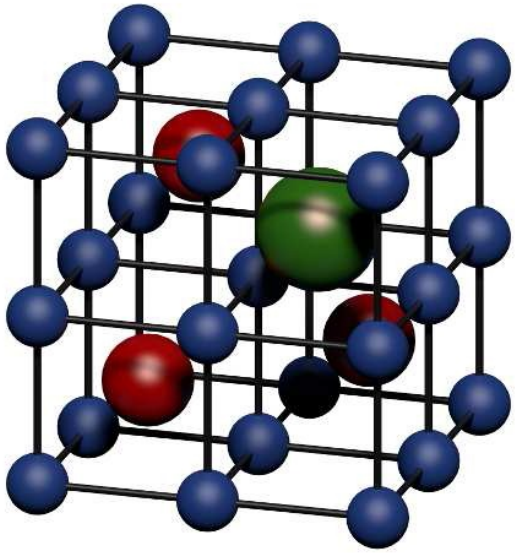

Figure 1.1: Illustration of the calcium fluoride crystal structure with calcium ions (red), fluoride ions (blue) and lanthanide dopant (green) [22].

$4f^{N-1}5d$ transitions are characteristically broad and the energies of these transitions change very noticeably, dependent on the host lattice. Due to the contraction of the wavefunction of the $4f$ orbital, these undergo reduced interaction with their surrounding environment and therefore the crystal field contribution to the energy level splitting is small in magnitude. As a result, these $4f^N$ - $4f^N$ transitions are very narrow and the energies of these transitions vary minimally between host lattices.

Three prominent single ion sites can arise in bulk CaF_2 crystals; O_h, $C_{4v}(F^-)$ (where (F^-) indicates the charge compensation coming from a fluoride ion), and $C_{3v}(F^-)$. In the $C_{4v}(F^-)$ site, the charge compensating F^- ion is in the empty fluoride cage adjacent to the europium ion, whereas its location in the $C_{3v}(F^-)$ site is in an empty fluoride cage diagonal to the europium ion. When light lanthanides are doped into CaF_2, the $C_{4v}(F^-)$ centre has been shown to be dominant, whilst the $C_{3v}(F^-)$ centre is not prominent [23]. Due to this, the only single-ion symmetries considered in this study will be O_h and $C_{4v}(F^-)$. The octahedral symmetry shown in Figure 1.2 is very simple, with only one europium ion, enclosed within a cage of eight fluoride ions. This centre has non-local charge compensation which is required due to the substitution of the Ca^{2+} ion for the Eu^{3+} ion. Normally, the tetragonal ($C_{4v}(F^-)$) centre is the dominant centre for low concentrations of Eu^{3+} ions in CaF_2.

Aside from single-ion symmetries, clustering of rare-earth ions occurs at regimes of higher dopant concentration. These clusters collect fluoride interstitials and result in a site of excess negative charge. Europium cluster centres are dominated by dimer and trimer configurations [24]. Figure 1.3 shows the observed cluster centres in CaF_2:Eu^{3+}. The Q centre arises as a result of three Eu^{3+} ions experiencing the same crystal field and is known as an equivalent trimer cluster. By contrast, Eu^{3+} ions in the R centre both experience different crystal fields and this configuration is referred to as an inequivalent dimer cluster.

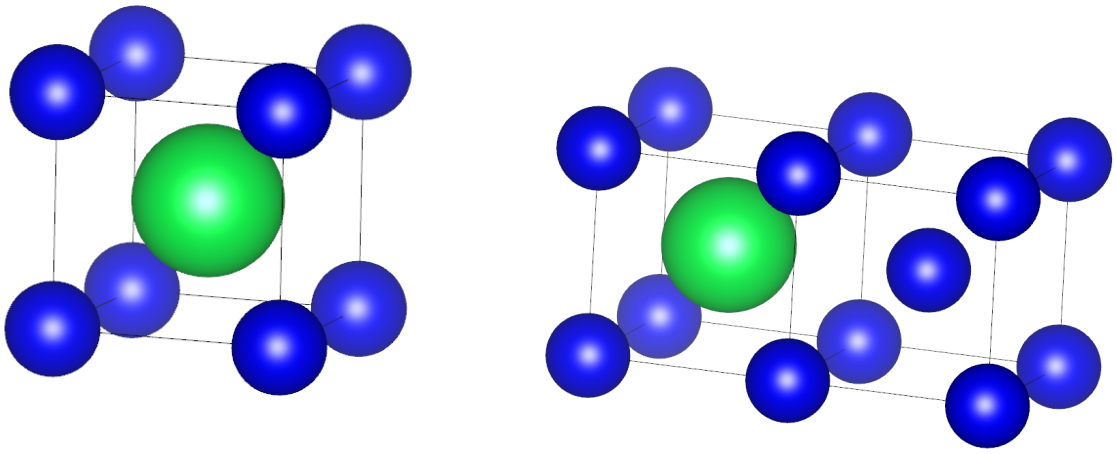

Figure 1.2: Illustration of the O_h centre of CaF_2:Eu^{3+} (left) and illustration of the $C_{4v}(F^-)$ centre of CaF_2:Eu^{3+} (right). The green sphere is the Eu^{3+} ion and the blue spheres are the surrounding F^- ions. The charge compensating fluoride ion is non-local for the O_h centre.

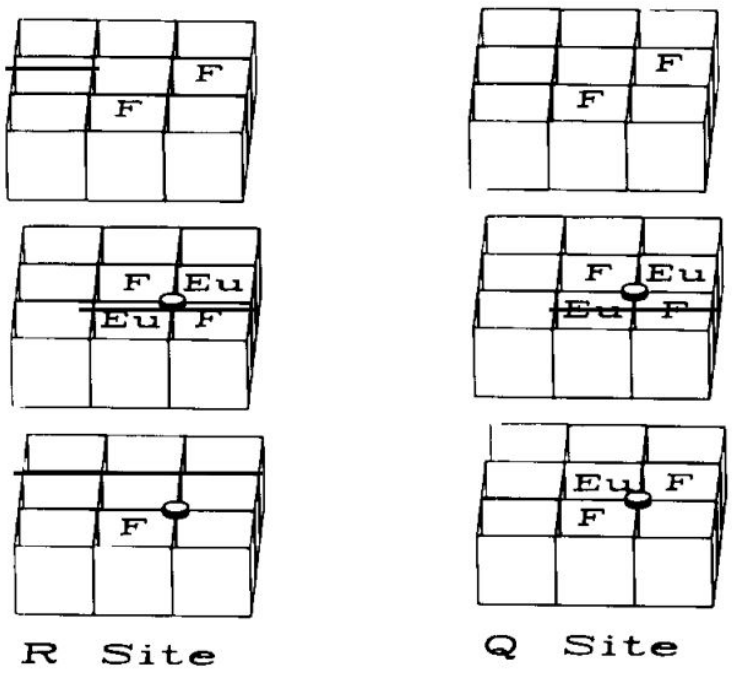

Figure 1.3: R and Q centres in CaF_2:Eu^{3+}. This schematic shows three layers of the site separately, which lie on top of one another to form a 9 x 9 structure of fluoride cages. Disks at intersections indicate fluoride vacancies [24].

CaF_2:Eu^{3+} can also been co-doped with monovalent sodium (Na^+). Na^+ charge compensated Eu^{3+} centres arise as a result of this codoping and are labelled as the $C_{2v}(Na^+)$ centre. In this case the Na^+ ion replaces a Ca^{2+} cation [25]. In general, this leads to a substantial reduction in centres other than the cubic and $C_{2v}(Na^+)$ centres.

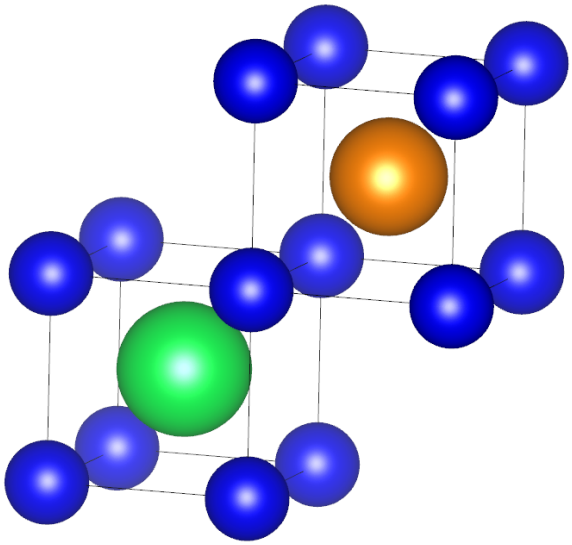

Figure 1.4: Illustration of the $C_{2v}(Na^+)$ centre in $CaF_2:Eu^{3+}:Na^+$. The green, orange, and blue spheres are the Eu^{3+} ion, Na^+ ion, and F^- ions respectively.

1.3 Laser Spectroscopy

The spectroscopy of rare-earth doped CaF_2 is complicated by the presence of multiple charge compensation configurations. Conventional spectroscopy (such as using lamps for absorption spectroscopy) is not site-selective and therefore spectroscopic information cannot be gathered that is correlated to a specific site within the crystal structure. If the absorption resonances of these different sites are sufficiently distinct, then a narrow-band laser can be used to excite a specific site within the crystal, while minimising absorption of other sites. The large intensity of light from a laser which is resonant with the transition energy causes a significant population of ions within the selected site to be excited, resulting in a higher emission signal than other non-selective means of excitation. Laser site-selective excitation was first demonstrated in 1975, by Tallant and Wright [26]. Since then, complex spectra such as that found in their published work on $CaF_2:Er^{3+}$ have utilised site-selective laser spectroscopy to separate these sites and analyse them appropriately. From their work in 1975, Tallant and Wright were able to study 16 sites within the crystal.

1.4 Outline of Thesis

This work presents a spectroscopic study of $CaF_2:Eu^{3+}$ nanocrystals, and compares the results to analogous studies of the bulk crystal. This was achieved using pulsed laser fluorescence spectroscopy, excitation spectroscopy and lifetime measurements of the available excited states. A tunable pulsed laser was used in order to be able to select the excited state for study. The nanoparticles were excited from its ground state ($^7F_0$) to both of the excited states $^5D_0$ and $^5D_1$ and it is these two emitting states, from which transitions were studied.

Chapter two outlines relevant crystal field theory and the physics governing energy shifts as observed in spectroscopic studies. This includes discussion of the free-ion Hamiltonian, which continues into the crystal-field Hamiltonian for a given centre. Effects due to the

nanoparticles' sizes are also discussed with final sections explaining the theory behind the transition intensities of rare-earth ions and using group theory to determine selection rules.

Chapter three describes the experimental procedure and the equipment that accompanies it, which includes the methods used to measure spectroscopic data from the sample in question. The first section explains the growth of bulk CaF_2:Eu^{3+} crystals, using an RF furnace. The second section describes the co-precipitation method used to synthesise the nanoparticles. The final sections describe the experimental procedures of both absorption spectroscopy and laser site selective spectroscopy used in this work.

Chapter four presents high-resolution excitation spectra from the ground state multiplet $^7F_0$ to both multiplets $^5D_0$ and $^5D_1$ for CaF_2:0.25%Eu^{3+} nanocrystal samples, cooled to 10 K. Three centres were observed for the $^5D_0$ multiplet, whereas four were observed for the $^5D_1$ multiplet. The results of high-resolution fluorescence spectroscopy are also presented, and many energy levels of the ^7F_J multiplets could be identified. Lifetimes for these excited states are presented. From these studies, both surface ion configurations as well as ions within the nanoparticle have been isolated.

Chapter five presents a summary of the work and discusses conclusions that can be drawn from these results. This chapter also makes suggestions for future experiments.

Chapter 2

Theory

2.1 Free Ion Hamiltonian

In a free ion system, the interactions which split the $4f^N$ configuration can be modelled using an interaction Hamiltonian [27]:

$$H_{\text{f.i.}} = \left[\frac{-\hbar^2}{2m}\sum_{i=1}^{N}\nabla_i^2 - \sum_{i=1}^{N}\frac{Ze^2}{r_i} + \sum_{i<j}^{N}\frac{e^2}{r_{ij}}\right] + \sum_{i=1}^{N}\zeta(r_i)l_i\cdot s_i \tag{2.1}$$

Equation (2.1) has several terms contributing to different physical interactions in this many-electron system. The first term represents the kinetic energy of each electron summed together, whereas the second term is the total electric potential energy. The third term is the Coulomb interaction term, which describes how each of the electrons repulse one another. The last term describes the total spin-orbit interaction of the system. However, a problem in solving this system is that the repulsion between the electrons is too big of a term to be able to deal with using perturbation theory. In order to solve this problem, the Hamiltonian can be rewritten by constructing a spherically symmetric potential energy function, represented by $U(r_i)$. This approximates the field experienced by one $4f$ electron, as a result of the nucleus and all other $4f^{N-1}$ electrons. The free ion Hamiltonian system can now be rewritten by including this central field approximation:

$$\begin{aligned} H_{\text{f.i.}} &= H_0 + H_{\text{coulomb}} + H_{\text{s.o.}} \\ &= \sum_{i=1}^{N}\left[\frac{-\hbar^2}{2m}\nabla_i^2 + U(r_i)\right] + \left[\sum_{i=1}^{N}\frac{-Ze^2}{r_i} - \sum_{i=1}^{N}U(r_i) + \sum_{i<j}^{N}\frac{e^2}{r_{ij}}\right] + \sum_{i=1}^{N}\zeta(r_i)l_i\cdot s_i \end{aligned} \tag{2.2}$$

The H_0 component of Equation (2.2) can now be solved for N electrons with solutions given as spherical harmonics:

$$\psi_{n,l,m_l,m_s}(r,\theta,\phi) = \frac{R_{nl}(r)}{r}Y_{l,m_l}(\theta,\phi)\chi_{m_s} \tag{2.3}$$

Equation (2.3) has three main components, beginning with the radial function $R_{nl}(r)$,

which is dependent on the central field $U(r_i)$. Y_{l,m_l} are spherical harmonics, reliant on both angles of θ and ϕ in a spherical polar coordinate system. Lastly, χ_{s,m_s} are the spin functions. This expression is further antisymmetrised and this is done in order to satisfy the Pauli exclusion principle, as electrons are fermions and must be antisymmetric with respect to inversion.

In dealing with the other components of Equation (2.2), the remaining terms $H_{coulomb}$ and $H_{s.o.}$ can be treated as perturbations of H_o. In terms of splitting degenerate configurations, the only two terms that contribute to this from Equation (2.2) are the Coulomb repulsion ($\sum_{i<j}^{N} \frac{e^2}{r_{ij}}$) and spin-orbit interaction ($\sum_{i=1}^{N} \zeta(r_i) l_i \cdot s_i$) terms.

The Coulombic repulsion term behaves by splitting the 4f configuration in terms known as free-ion terms, denoted by ^{2S+1}L. The magnitude of this splitting is generally in the order of 10000 cm^{-1}. Spin-orbit coupling is a relativistic effect and can be described as the interaction between the magnetic component of an electron's spin and the magnetic field produced by the orbital motion of the same electron. This splits the ^{2S+1}L terms into $2S+1$ terms. Each of these new terms have a $2J+1$ fold degeneracy, being given new labels of $^{2S+1}L_J$. The magnitude of this interaction is generally within the magnitude of 1000 cm^{-1}.

2.2 Crystal Field Theory

A free ion has spherical symmetry when isolated from external sources. However, when the ion is placed within a crystal structure, the ion's symmetry is lowered, based on its location in the crystal lattice. As a result, these neighbour ions in the lattice have an electromagnetic influence on the energies on the $4f^{\mathrm{N}}$ orbital, splitting the free ion levels further. This splitting is smaller in magnitude than the spin-orbit interaction and can also be treated as a perturbation (as done with the earlier free-ion calculations). In a $4f^{\mathrm{N}}$ configuration in lanthanide ions, the $4f$ orbital is contracted further towards the nucleus, becoming shielded by the $5s^2$ and $5p^6$ orbitals. By employing the central field approximation in order to get Equation (2.2), the new Hamiltonian can now be given in the below form, where the crystal field can be treated as a perturbation of the free-ion Hamiltonian:

$$H = H_{\mathrm{f.i.}} + H_{\mathrm{c.f.}} \tag{2.4}$$

The crystal field Hamiltonian can be expressed of spherical harmonics, or in terms that transform as spherical harmonics [28]:

$$H_{\mathrm{c.f.}} = \sum_{k,q,i}^{N} B_q^k (C_q^{(k)})_i \tag{2.5}$$

Equation (2.5) shows the sum of the crystal field perturbations over all N electrons in the $4f^N$ orbital of the lanthanide ion. Non-zero values of B_q^k result from the triangular rule for addition of angular momentum, as well as parity considerations. If only considering a state of a single configuration ($4f^N$), then a further constraint can be placed on the parameter k, giving the range $2l \geq k \geq 0$. $k = 0$ can be neglected, as it does not contribute to splitting, only to a uniform shift for all energy levels. In free-ion terms, the f orbital has a quantum

number of $l = 3$. Therefore, the upper-limit for the k parameter would be 6. Using these parameters, B_q^k is used as a parametrisation of the strength of the crystal field acting on the lanthanide ion. The $C_q^{(k)}$ are called the Racah spherical tensor operators and can be related to the spherical harmonics $Y_{k,q}$, which is similar to the spherical harmonic given in Equation (2.3). This is given by

$$\begin{aligned} C_q^{(k)} &= \sqrt{\frac{4\pi}{2k+1}} Y_{k,q}(\theta, \phi) \\ &= (-1)^q \sqrt{\frac{(k-q)!}{(k+q)!}} r^k P_{k,q}(\cos(\theta))(\cos(\phi) + i\sin(\phi)) \end{aligned} \tag{2.6}$$

where the $P_{k,q}(\cos(\theta))$ term is the Legendre polynomial and is defined as

$$P_{k,q} = \frac{(1-\cos\theta^2)^{q/2}}{2^k k!} \frac{d^{(k+q)}}{d\cos\theta^{(k+q)}} (\cos\theta^2 - 1)^k \tag{2.7}$$

By employing the Wigner-Eckart Theorem, matrix elements for the interaction term can be calculated from a given crystal-field Hamiltonian. Given a tensor operator $T_q^{(k)}$ and two angular momenta states j and j', the Wigner-Eckart theorem can be used as shown:

$$\langle jm|T_q^{(k)}|j'm'\rangle = \langle j'm'kq|jm\rangle \, \langle j||T^{(k)}||j'\rangle \tag{2.8}$$

Given Equation (2.8), the $|jm\rangle$ term gives the eigenstate of both total angular momentum J^2 and its corresponding z-axis component, J_z. $\langle j'm'kq|jm\rangle$ is the Clebsh-Gordan coefficient, which describes the coupling of j, k, and j'. The final term $\langle j||T^{(k)}||j'\rangle$ shows a value that is independent of m, m', or q and is known as the reduced matrix element.

A given crystal-field Hamiltonian can have its matrix elements calculated by using the following:

$$\langle \alpha SLJM|H_{c.f.}|\alpha' SLJ'M'\rangle = \sum_{k,q} \langle \alpha SLJM|U_q^k|\alpha' SLJ'M'\rangle \times \langle l||C^{(k)}||l\rangle \tag{2.9}$$

The variable α is a representation of all other quantum numbers that are used to specify the state (and are not important to these crystal field calculations). $\langle l||C^{(k)}||l\rangle$ is a reduced matrix element and can be given [29] by:

$$\langle l||C^{(k)}||l\rangle = (-1)\sqrt{(2l+1)(2l'+1)} \begin{pmatrix} l & k & l' \\ 0 & 0 & 0 \end{pmatrix} \tag{2.10}$$

The last factor in Equation (2.10) is called the Wigner 3-j symbol and can is related to the Clebsch-Gordon (CG) coefficients [30]. In general, Wigner 3-j symbols can be related to C-G coefficients by:

$$\begin{pmatrix} j_1 & j_2 & j_3 \\ m_1 & m_2 & m_3 \end{pmatrix} = \frac{(-1)^{j_1-j_2-m_3}}{\sqrt{2j_3+1}} \langle j_1 m_1; j_2 m_2 | j_1 j_2; j_3 - m_3 \rangle \tag{2.11}$$

These 3-j symbols can be complicated to calculate. However, tabulated 3-j symbols are given by Rotenberg et al. [31]. By applying the Wigner Eckart theorem, J and M dependence can be removed from the matrix elements of the crystal field perturbation:

$$\begin{aligned} \langle \alpha SLJM | U_q^k | \alpha' SL'J'M' \rangle = (-1)^{J-M} \sqrt{(2J+1)(2J'+1))} \begin{pmatrix} J & k & J' \\ -M & q & M' \end{pmatrix} \\ \times \langle \alpha SLJ || U^k || \alpha' SL'J' \rangle \end{aligned} \tag{2.12}$$

This first step only removes M dependence from the matrix elements. To remove J dependence from the matrix elements, the Wigner 6-j symbol (which can also be found tabulated with the 3-j symbols [31]) can be used [28]:

$$\langle \alpha SLJ || U^k || \alpha' SL'J' \rangle = (-1)^{S+L'+J+k} \sqrt{(2J+1)(2J'+1)} \begin{Bmatrix} J & J' & k \\ L' & L & S \end{Bmatrix} \times \langle \alpha SL || U^k || \alpha' SL' \rangle \tag{2.13}$$

Like the 3-j and 6-j symbols, the reduced matrix elements are time-consuming to manually calculate each time and so these have also been tabulated by Nielson and Koster [32]. Depending on the crystal field symmetry, different tensors are used for the crystal field operator. For example, an axial operator C_0^k have no splitting effects on the z-axis angular momentum eigenvalues m and will simply shift the energy levels, with no m degeneracies broken. However, C_q^k operators only have a non-zero matrix element when the relationship $M - M' = q$ is satisfied. As a result, states that are degenerate with magnetically sensitive substates are split as a result of this q-dependent operator. Due to this splitting and mixing of states that satisfy the mentioned relationship, the quantum numbers J and M are no longer good candidates for labelling states. Instead, group theory can be employed and irreducible representations (irreps) of the appropriate point group (based on local symmetry) can be used as labels for these new, mixed electronic states.

The crystal field expression can be simplified as a result of the local symmetry. The $C_{4v}(F^-)$ centre of CaF_2:Eu^{3+} can have its corresponding crystal field Hamiltonian expressed as [33]

$$\begin{aligned} H_{C_{4v}} = B_A^2 C_0^{(4)} + B_A^4 \left[C_0^4 - \sqrt{\frac{7}{10}} (C_4^{(4)} + C_{-4}^{(4)}) \right] + B_A^6 \left[C_0^{(6)} + \sqrt{\frac{1}{14}} (C_4^{(6)} + C_{-4}^{(6)}) \right] \\ + B_C^4 \left[C_0^{(4)} + \sqrt{\frac{5}{14}} (C_4^{(4)} + C_{-4}^{(4)}) \right] + B_C^6 \left[C_0^{(6)} - \sqrt{\frac{7}{2}} (C_4^{(6)} + C_{-4}^{(6)}) \right] \end{aligned} \tag{2.14}$$

where the B_C^k parameters describe the cubic influences to the crystal field effect and where the B_A^k parameters describe the magnitude of the tetragonal distortions. This originates due

to tetragonal symmetry being a distorted form of cubic symmetry, where the cubic lattice is stretched along one of its lattice vectors. The final two terms of this Hamiltonian are equivalent to the crystal field Hamiltonian for a cubic symmetry.

2.3 Nanoparticle Size Effects

There may be a significant difference between the optical properties of bulk materials and their nanomaterial counterparts. In terms of this study (lanthanide-doped nanoparticles), this small particle size may have a drastic effect on the lifetime of excited metastable states or the quantum yield of luminescence (which is the ratio of photons emitted to photons absorbed) [10]. This can be attributed to two of the biggest changes that will occur from the transition from bulk material to nanomaterial; any structural distortion as a result of a reduced size and surface defects.

Due to the localisation of $4f$ electronic states, no quantum confinement effects should be occur in the energy-level structure associated with lanthanide ions [15]. However, the optical dynamics in lanthanide-doped dielectric NPs can undergo significant alteration due to the presence of electron-phonon interactions. This is important as in NPs the phonon density of states (PDOS) is discrete. As a direct result of this discretisation, acoustic phonon modes are cut off, leaving only the optical modes. Due to this modification of the PDOS, there is an expected difference in both luminescence and non-radiative relaxation from the excited states. The cut-off frequency for phonon modes $\nu_{\min}$ can be expressed as

$$\nu_{\min} = \frac{\nu_{\mathrm{t}}}{2\pi R}\eta_{\min} \tag{2.15}$$

where $\eta_{\min} = 2.05$ and is the minimal reduced frequency, R is the radius of the nanoparticles, and ν_{t} is the sound frequency of the transverse mode [15].

One direct result of phonon-electron interactions is the broadening of line widths of electronic transitions. Line broadening exists in two types; homogeneous and inhomogeneous. Inhomogeneous is a result of structure defect and strain-induced variation in electronic energy levels. Homogeneous line broadening is temperature dependent and can therefore be directly linked with the PDOS present in a crystalline structure, as the PDOS is temperature dependent itself. De-excitation times of excited states τ can be expressed as $\tau = (\pi\Gamma)^{-1}$, where Γ is the homogeneously broadened line width. There also exists a temperature-dependent shift in energy of the electronic transitions. The homogeneous line width Γ and energy shift δE of a two level electronic transition can be expressed by the following McCumber-Sturge [34] equations:

$$\Gamma = \Gamma_0 + \bar{\alpha}\left(\frac{T}{T_D}\right)^7 \int_0^{T_D/T} \frac{x^6 e^x}{(e^x-1)^2} dx \tag{2.16}$$

$$\delta E = \alpha\left(\frac{T}{T_D}\right)^4 \int_0^{T_D/T} \frac{x^3}{e^x-1} dx \tag{2.17}$$

Equations (2.16) and (2.17) describe the temperature dependence on both line width

and energy shift, respectively. In those equations, Γ_0 represents the residual width and is temperature independent and a result of strain on the crystal. $\bar{\alpha}$ and α are electron-phonon coupling coefficients and T_D is the effective Debye temperature. Both of the coupling coefficients and the Debye temperature can be treated as free parameters in fitting algorithms to best fit some given experimental data. By extrapolating the data to 0 K, the residual line width and position can be estimated.

2.4 Spectroscopic Intensities in Rare-Earth Ions

Optical excitation of lanthanide ions occurs via the interaction of the incoming electromagnetic wave with either the electric dipole or magnetic dipole moments of the ion. As the magnetic dipole interaction is a second order effect, the electric dipole moments are typically larger in magnitude. Selection rules differ depending on the dipole interacting in the excitation. The electric dipole operator forbids $4f^N \rightarrow 4f^N$ transitions, due to the odd parity of the electric dipole operator. Admixture of even parity wavefunctions are required to observe these transitions via the electric dipole interaction and can be found in crystal field symmetries, due to uneven terms in the crystal field Hamiltonian. The electric dipole operator, when given as a tensor, has the form:

$$P_\rho^{(1)} = -e \sum_{\rho,i} r_i (C_\rho^{(1)})_i \tag{2.18}$$

This is a rank 1 tensor, where $\rho = 0$ represents the z-component, and $\rho = \pm 1$ for the x$\pm$iy components, each representing different polarisations of the laser light. This operator can be taken and applied to an overlap of two states (each of mixed parity)

$$\langle A|P_\rho^{(1)}|B\rangle = -\sum_\kappa \frac{\langle JM|V|\kappa\rangle \langle \kappa|P_\rho^{(1)}|J'M'\rangle}{E_{JM} - E_\kappa} - \sum_\kappa \frac{\langle JM|V|\kappa\rangle \langle \kappa|V|J'M'\rangle}{E_{J'M'} - E_\kappa} \tag{2.19}$$

where the two states are defined as:

$$\langle A| = \langle JM| - \sum_\kappa \frac{\langle JM|V|\kappa\rangle \langle \kappa|}{E_{JM} - E_\kappa}$$
$$\langle B| = \langle J'M'| - \sum_\kappa \frac{|\kappa\rangle \langle \kappa|V|J'M'\rangle}{E_{J'M'} - E_\kappa}$$

In this expression, κ denotes that all the perturbed states are being summed over and the states $\langle JM|$ and $|J'M'\rangle$ are states which are admixed by the crystal field. An approximation can be made regarding the denominator terms that $E_{JM} - E_\kappa = E_{J'M'} - E_\kappa = E_{avg}$, and then approximate that $\sum_\kappa |\kappa\rangle \langle \kappa|$ is equal to unity [35]. Continuing,

$$\langle A|P_\rho^{(1)}|B\rangle = \sum_{\lambda,q} Y(\lambda, q, \rho) \langle f^N \alpha S L J M | U_{\rho+q}^{(\lambda)} | f^N, \alpha' S' L' J' M'\rangle \tag{2.20}$$

in which

$$Y(\lambda,q,\rho) = -\frac{2}{E_{avg}}\sum_{k}(-1)^{q+\rho}(2\lambda+1)\begin{pmatrix}1 & \lambda & k\\ \rho & -(q+\rho) & q\end{pmatrix}\begin{pmatrix}l & l & k\\ 1 & k & l'\end{pmatrix} \times \langle l||C^{(1)}||l'\rangle \langle l'||C^{(k)}||l\rangle B_q^k e\int R_{nl}(r) r R_{n'l'}(l) dr \tag{2.21}$$

By using Equation (2.21), selection rules can be collected by applying the triangular rules for the addition of angular momentum, which can be done using the 3j and 6j symbols. In general, selection rules for electric-dipole transitions are as follows:

$$\Delta l = \pm 1$$
$$\Delta S = 0$$
$$|\Delta L|, |\Delta J| \leq 2l$$

However, when a rare-earth ion is situated in a crystal lattice, the crystal field causes mixing of J states, breaking down these selection rules, which has been shown by Lowther [36]. In the case in which a state involved is J = 0, then only J = 2,4 or 6 is accessible by using the electric dipole transition.

Magnetic dipole transitions are much simpler due to the much more simple dipole operator of $(L + 2S)$, which is of even parity. Its matrix elements can be calculated in the same fashion:

$$\langle f^N \alpha S L J M | L + 2S | f^N \alpha' S' L' J' M' \rangle = (-1)^{J-M}\begin{pmatrix}J & 1 & J'\\ -M & \rho & M'\end{pmatrix} \times \langle f^N \alpha S L J || L + 2S || f^N \alpha' S' L' J' \rangle \tag{2.22}$$

Using the same rules as for the electric dipole transitions, the selection rules are:

$$\Delta l = 0$$
$$\Delta S = 0$$
$$\Delta L = 0$$
$$\Delta J = 0, \pm 1$$

However, an exception to the selection rule here is that while ΔJ can be equal to 0, transitions between two states of $J = 0$ are not allowed. In both cases (electric and magnetic dipole transitions), these selection rules are subject to relaxation under the conditions of spin-orbit coupling mixing into admixtures of states. The spin-orbit interaction breaks down the $\Delta S = 0$ selection rule.

2.5 Symmetry & Spectroscopic Selection Rules

The resultant $4f$ wavefunctions due to the crystal field environment interaction can be assigned irreducible representations (irreps), appropriate to the symmetry point group for which the wavefunctions were derived. For a transition between two energy states to occur, the two respective wavefunctions must have a degree of overlap, which can be defined as:

$$\langle \phi_j^* | \sigma_\mathrm{o} | \phi_i \rangle$$

where σ_o in this case is the operator related to the relevant dipole moment (either electric or magnetic). This overlap integral must be non-zero in order for there to be an allowed transitions between the two energy states via the diople operator specified. In terms of group theory, the direct product of the character of the operator and the character of the initial state must include the character of the final state:

$$\Gamma_\mathrm{o} \otimes \Gamma_i \supset \Gamma_j$$

For this to be possible, the operator must transform as an irrep (or irreps) of the symmetry in which the transition is occurring and that the wavefunctions have been derived for. For example, if the wavefunction of the excited state transforms as γ_1, then the direct product of the irreps that the initial wavefunction and the operator transform as must contain γ_1 for the transition to be allowed, where γ_1 is an irrep.

Independent of symmetry, the electric dipole operator transforms as the cartesian basis (x,y,z) as the magnetic dipole transforms as the rotational basis (R_x, R_y, R_z). Different irreps represent these bases, dependent on symmetry. In a $C_{4\mathrm{v}}$ symmetry, the electric dipole operator transforms as $\mathrm{A}_1 \oplus \mathrm{E}$ and the magnetic dipole operator transforms as $\mathrm{A}_2 \oplus \mathrm{E}$. It can be seen by this that both dipole operators share an irrep in their transformations, E. From this, character tables can be made, showing which transitions are allowed, dependent on the dipole operator being applied and at what orientation the dipole is incident to the axes. The $\mathrm{C}_{4\mathrm{v}}$ group has 5 irreps and can be shown in the following character table [37]:

Table 2.1: Character table for $\mathrm{C}_{4\mathrm{v}}$ point group

	E	$2\mathrm{C}_4$	C_2	$2\sigma_\mathrm{v}$	$2\sigma_\mathrm{d}$	Transformations
$\mathbf{A}_1$	1	1	1	1	1	z, $x^2 + y^2$, z^2
$\mathbf{A}_2$	1	1	1	-1	-1	R_z
$\mathbf{B}_1$	1	-1	1	1	-1	$x^2 - y^2$
$\mathbf{B}_2$	1	-1	1	-1	1	xy
$\mathbf{E}$	2	0	-2	0	0	(x, y), (R_x, R_y), (xz, yz)

To attain the numbers given in Table 2.1, a matrix must be constructed which reflects the symmetry operation performed in a given coordinate system (for example, in cartesian coordinates). The trace of this matrix is then taken and this is called the character of the symmetry operation. The products of these irreps can then be calculated by multiplying the characters for each symmetry operation separately, which gives the following product table:

Table 2.2: Product table for C_{4v} point group

	$\mathbf{A_1}$	$\mathbf{A_2}$	$\mathbf{B_1}$	$\mathbf{B_2}$	**E**
$\mathbf{A_1}$	A_1	A_2	B_1	B_2	E
$\mathbf{A_2}$	A_2	A_1	B_2	B_1	E
$\mathbf{B_1}$	B_1	B_2	A_1	A_2	E
$\mathbf{B_2}$	B_2	B_1	A_2	A_1	E
E	E	E	E	E	$A_1 \oplus A_2 \oplus B_1 \oplus B_2$

The electric dipole operator transforms as $A_1 \oplus E$ and the magnetic dipole operator transforms as $A_2 \oplus E$. By operating both the electric dipole (ED) and the magnetic dipole (MD) operators onto the irreps, spectroscopic selection rules can be obtained :

Table 2.3: Table of selection rules for C_{4v} point group

j^{th} state	i^{th} state				
	$\mathbf{A_1}$	$\mathbf{A_2}$	$\mathbf{B_1}$	$\mathbf{B_2}$	**E**
$\mathbf{A_1}$	ED	MD	-	-	ED, MD
$\mathbf{A_2}$	MD	ED	-	-	ED, MD
$\mathbf{B_1}$	-	-	ED	MD	ED, MD
$\mathbf{B_2}$	-	-	MD	ED	ED, MD
E	ED, MD	ED, MD	ED, MD	ED, MD	ED, MD

Chapter 3

Experimental Techniques

3.1 Crystal Growth and Preparation

Bulk CaF_2:Eu^{3+} crystals were grown at the University of Canterbury. The starting material was prepared by crushing up offcuts of CaF_2, and mixing it with the appropriate amount of EuF_3. A small amount of PbF_2 was added to the charge in order to act as an oxygen scavenger, also resulting in a crystal with reduced concentration of the divalent species of europium. The divalent species arise because of the reducing environment provided by the graphite crucible. In this study, results from the nanoparticles will be compared to analogous bulk crystals, which were grown using this method.

Figure 3.1: Picture of the RF furnace used to grow bulk crystals.

The crystals were grown in a graphite crucible over 24 hours, using a 38 kW radio frequency (RF) furnace. The singularly doped CaF_2:Eu^{3+} crystal was grown in a vacuum, whereas the sodium doped crystal was grown in an argon atmosphere. The Bridgman tech-

nique was used, where a temperature gradient is generated by a current flowing through coils, which causes inductive heating on the crucible as it is lowered. By bringing the crucible outside of the induction coils, the crucible starts to cool, which achieves annealing. This annealing process improves the quality of the resultant crystal. The produced crystals had a faint purple colour of varying intensity. This was due to some of the divalent species of europium left over from the crystal growth process and it having a visible purple colour due to electric dipole allowed $4f^N \rightarrow 4f^{N-1}5d$ transitions that are observable in Eu^{2+}.

For absorption measurements, the boule was prepared by first cutting off either end with a diamond saw and the ends were polished by different grades of sandpaper, completed by polishing with diamond paper. For smaller samples required for laser spectroscopy, thin slices ($\approx$ 2 mm) were cut off of the end of the boule and polished in the same manner as the boule. The nanoparticles were prepared by initially drying them in an oven and were then packed tightly into a copper mount with a hole placed into it to hold the nanoparticles. Once they were placed, a clean calcium fluoride crystal slice was placed over the top and stuck with silver paste. CaF_2 was chosen as a cover as it is transparent to visible light, which was being used to excite the nanoparticles.

3.2 Synthesis of CaF_2:0.25%Eu^{3+} Nanocrystals

The nanocrystals were grown in Fuzhou, China, with particle diameters being <10 nm. The method used to synthesise the nanocrystals used in this work is known as high-temperature co-precipitation, which is shown to be able to produce very high quality core-only nanoparticles. This method of synthesis offers the advantage of a fast growth rate, while not needing expensive equipment or complex procedures. Further treatment is usually required as a trade-off to the cheapness and ease of this process.

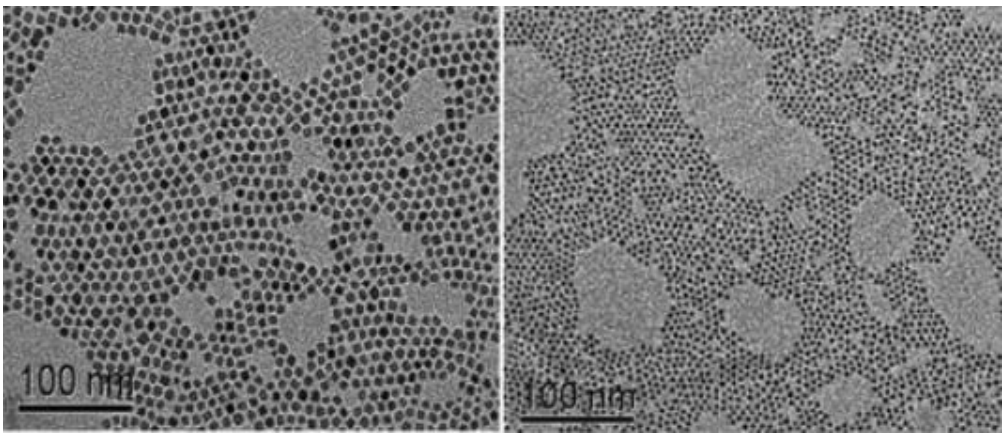

Figure 3.2: TEM images of RE^{3+}-doped CaF_2 nanocrystals [15].

Firstly, an alkaline earth metal trifluoroacetate precursor is prepared from the corresponding carbonates or oxides, which in this case produced calcium trifluoroacetate. This is typically done by adding in a slight excess of calcium carbonate/calcium oxide to the trifluoroacetatic acid, along with the application of heat and stirring, in order to make the reaction occur at a faster pace. This mixture is then typically stood overnight. Afterwards, the excess carbonate/oxide is filtered, giving a transparent calcium trifluoroacetate solution.

This is then dried in an oven, producing a powdered form of the calcium trifluoroacetate.

In a typical synthesis [38], 1 mmol of the resultant calcium trifluoroacetate power is added to a three-neck round-bottom vessel with 10 mL of coordinating solvent oleylamine (OM). 0.25 mmol of europium trifluoroacetate is also added to this vessel. The mixture is then heated to 100 °C under a constant flow of N_2 gas, where it is magnetically stirred for 30 minutes in order to remove residual water and oxygen. A colourless transparent solution is then obtained and rapidly heated to 280 °C under a nitrogen atmosphere, which is maintained for 1 hour. After this, the solution cools to room temperature and the nanoparticles are isolated from the rest of the solution via centrifuging and washed with ethanol 3 times. They are then dried in an oven at 80 °C for 1 hour.

3.3 Absorption Spectroscopy of Bulk CaF_2:Eu^{3+}

Long crystal boules were placed within a closed cycle cryostat and cooled to 10 K, which was then placed into the Cary 6000i Spectrophotometer. The Cary spectrometer consists of three separate lamps, which are optimised for providing differing wavelengths of light. These lamps are used in order to measure the absorption of a material placed within the Cary at a variation of wavelengths, ranging from the ultra-violet (UV) to the near infra-red (NIR), covering the visible part of the spectrum (Vis). There are two detectors, one of which does not have the sample between itself and the lamp, enabling calculation of absorption intensities. As the detector changes the detection wavelength, lamps change to efficiently provide the light required to detect the absorption at the appropriate wavelength.

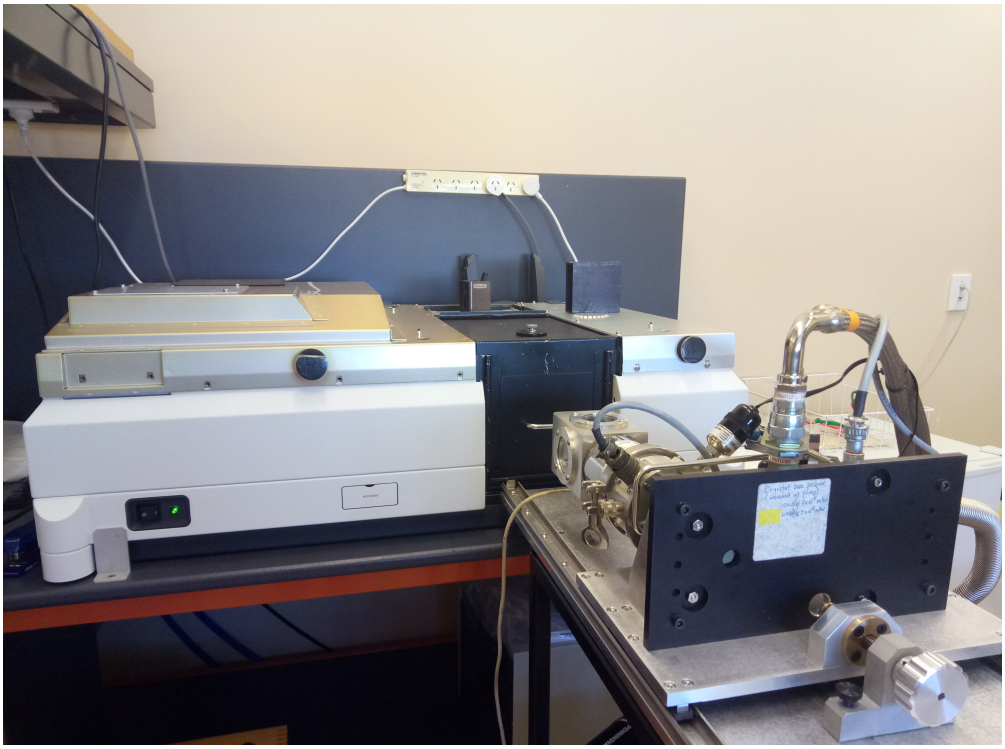

Figure 3.3: Picture of the Cary 6000i spectrophotometer used to gather absorption data from bulk CaF_2:Eu^{3+}.

3.4 Laser Spectroscopy

The nanoparticle sample in this experimentation was optically stimulated by a Model OL-402 pulsed N_2 laser pumped dye laser. A bank of capacitors in the laser is discharged and from that, the nitrogen gas inside a chamber in the laser is excited and causes lasing at 337 nm. Dye gain medium (Coumarin 500 or Rhodamine 6G) were used such that an appropriate wavelength could be chosen for the laser and it would be able to excite the nanoparticle sample. From here, the laser beam was directed towards the nanoparticle sample and the light emitting from the nanoparticles were directed towards the HR-640 spectrograph monochromator, which has a Czerny-Turner configuration with an 1800 lines per mm diffraction gratings. The light enters into the entrance slit and then leaves through the exit slit. The light then passes into a photomultiplier tube (PMT), with the signal from that entering the Hamatsu C8855-01 photon counter. The photon counter, which is connected to the computer via USB, enables the computer to save the data gathered through a LabVIEW VI. Slit widths were within the range of 100-250 μm.

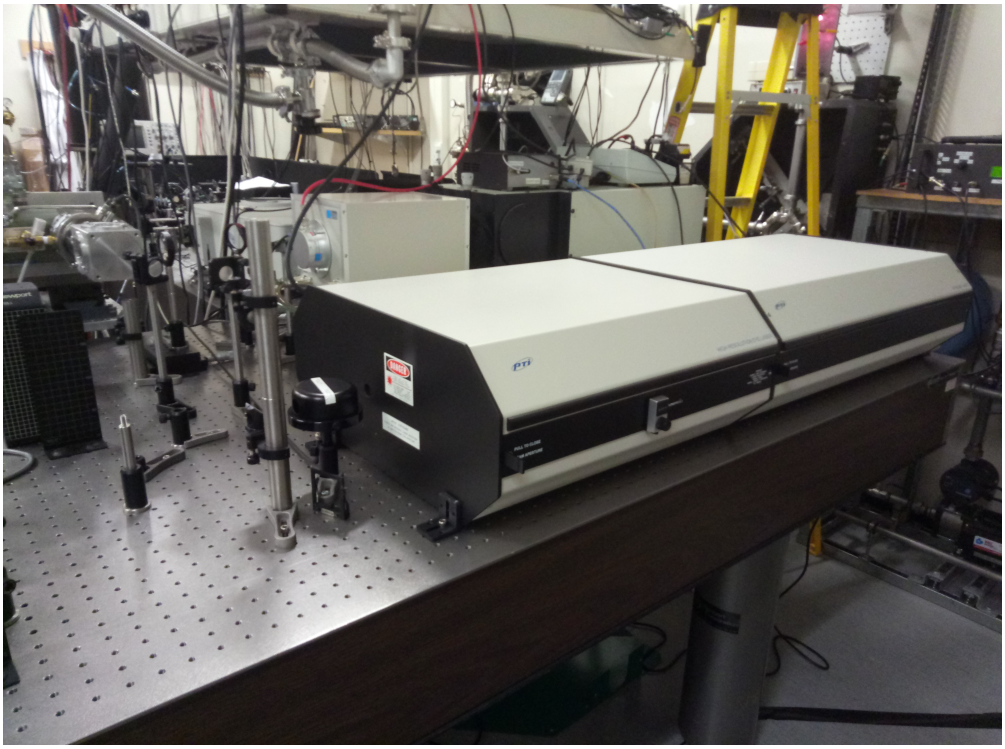

Figure 3.4: Picture of the nitrogen laser and dye laser.

The nanoparticle sample was cooled down to 10 K using a closed-cycle cryostat, in order to reduce the influence of non-radiative relaxation and minimise the optical linewidths. The PMT was also cooled to -25 °C with a peltier cooler to reduce thermal noise. Both the dye laser and the HR-640 had driver systems which allowed for computer automated data acquisition. This was performed using LabVIEW. In fluorescence measurements, the laser was manually tuned in order to optimise a strong fluorescence signal and the spectrometer was stepped by command of the computer to collect data. In excitation, a particular fluorescence peak was chosen and monitored by the spectrometer, while the laser controller stepped through a selection of wavelengths in order to collect the excitation data. Excitation spectroscopy was performed as both 'narrowband' and 'broadband' excitation. In narrowband

excitation, the spectrometer monitored a fluorescence transition associated with a distinct spectroscopic centre. By contrast, broadband excitation was obtained by monitoring all transitions to a given multiplet. Neutral density filters were placed in front of the spectrometer entrance slit to reduce to risk of increased photon counts damaging the PMT, as required.

Fluorescence lifetimes were measured at 10 K by a Tektronix DPO 7104 Digial Phosphor Oscilloscope to store the output of the PMT, which was triggered by the nitrogen laser pulse. 1000 samples were averaged to produce high resolution time-resolved fluorescence data for each transition monitored. Data for each monitored transition was then fitted with a single exponential in order to determine the fluorescence lifetime.

Chapter 4

Results & Analysis

In this study, Eu^{3+} transitions from the excited multiplets $^5D_0$ and $^5D_1$, down to the ^7F_J multiplets were measured. The powdered nanoparticle samples were cooled to 10 K for the purpose of these studies. As well as multiple excitation and luminescence spectra being recorded, lifetimes for each Eu^{3+} site were measured at 10 K. Due to the broad nature of these transitions, Gaussian fits were employed to give positions of transition energies. These nanoparticles, grown through the standard method, have a diameter of <10 nm. These sizes vary, as do the strains applied to each individual nanocrystal. This leads to the line broadening observed in this spectroscopic study. Gaussian fits were used in this work to attempt to de-convolute the many overlapping broad peaks present in the fluorescence spectra.

4.1 $^5D_0$ Excitation and Fluorescence

4.1.1 $^5D_0$ Excitation

Figure 4.1(a) shows the 10 K fluorescence detected absorption spectrum. This was obtained by exciting to the $^5D_0$ multiplet with Rhodamine 6G dye, monitoring all $^5D_0 \rightarrow {}^7F_2$ transitions. The spectrum observed displays heavily broadened spectral lines, due to sample inhomogeneities. A multicomponent Gaussian fit was employed in order to deconvolve individual spectral components associated with distinct spectroscopic centres. This fit has the form

$$\sum_{i}^{N} a_i \mathrm{e}^{-\left(\frac{(x-b_i)}{c_i}\right)^2} + d$$

where N is the number of Gaussian peaks applied to the spectra, a is the amplitude of the peak, b is the position, c is the full-width half maximum (FWHM), and d is the y-axis offset.

Three distinct spectral peaks can be observed in Figure 4.1(a). Figures 4.1(b)-(d) show the site selective excitation spectra obtained by monitoring fluorescence at 16327, 16090, and 16419 cm^{-1} respectively. The observed spectra are in reasonable agreement with the fitting to the experimental broadband excitation spectrum, although complete site selectivity has

not been obtained. In this work, we have arbitrarily labelled the individual spectroscopic centres as sites 1, 1a, and 2. It is notable that spectral selectivity against site 1a is very difficult to achieve. Table 4.1 gives the measured optical frequencies of the $^7F_0 \rightarrow {}^5D_0$ transitions for each centre.

Table 4.1: 10 K excitation frequencies for the $^5D_0$ multiplet in CaF_2:0.25%Eu^{3+} nanoparticles. The excitation frequencies were measured in air (cm^{-1}), with an uncertainty of ± 1 cm^{-1}.

Centre	Transition	Optical Frequency (cm^{-1})
Site 1	$Z_1 \rightarrow A_1$	17249
Site 1a	$Z_1 \rightarrow A_1$	17255
Site 2	$Z_1 \rightarrow A_1$	17274

The analogous CaF_2:Eu^{3+} bulk crystal has been measured to have Eu^{3+} centres located at 17259 [39], 17262 [39], 17274 [40], and 17288 cm^{-1} [39]. These centres are R (inequivalent dimer), Q (equivalent dimer), O_h, and $C_{4v}(F^-)$ sites respectively. The excitation frequencies observed in this work are within the range of cluster excitation frequencies, with site 2 matching that of the cubic site in the bulk crystal. Although it is noted that in the bulk crystal the cubic centre resonance is not observable for direct excitation of $^5D_0$.

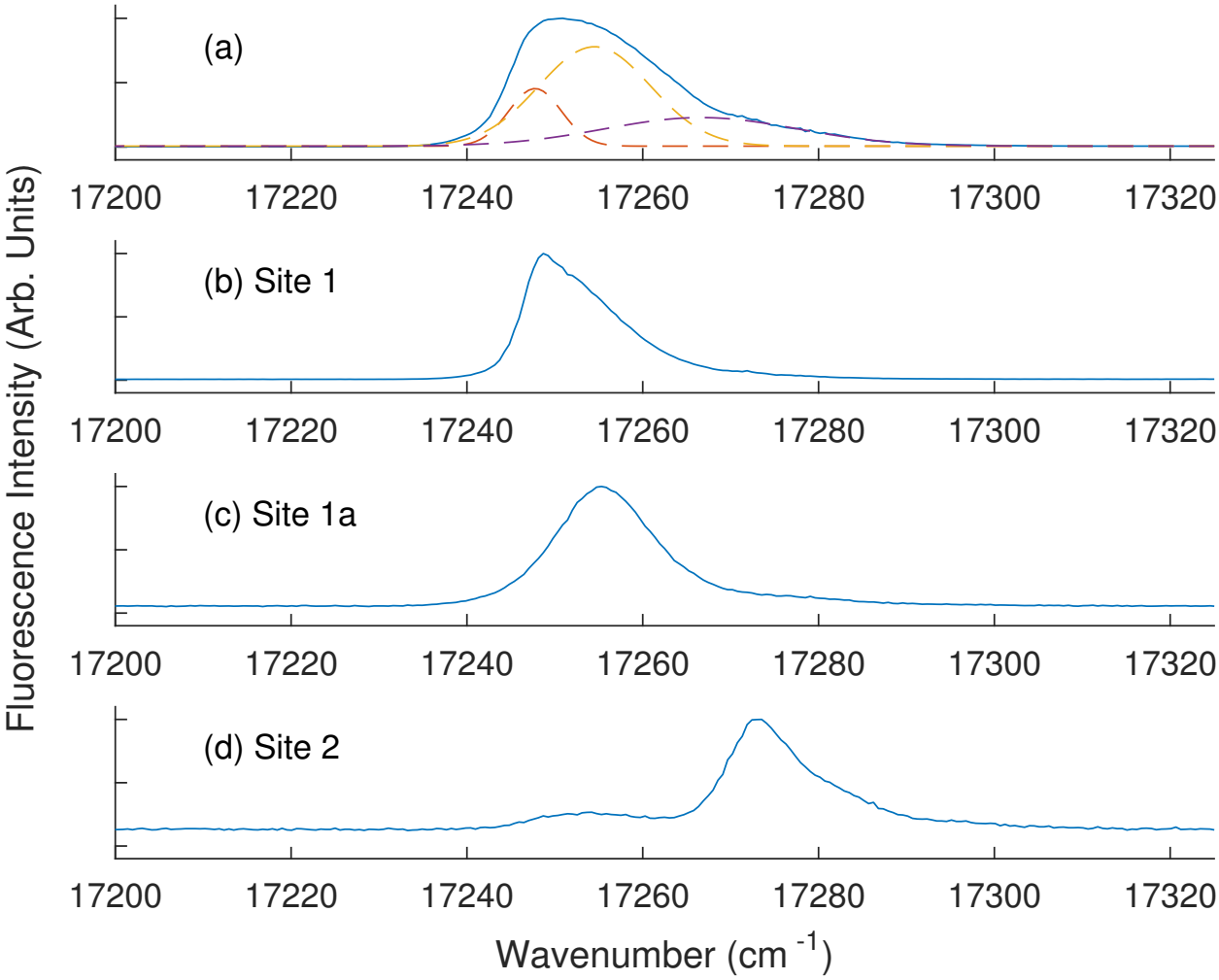

Figure 4.1: (a) 10 K broadband excitation of CaF_2:0.25%Eu^{3+} nanoparticles with the spectrometer monitoring all $^5D_0 \rightarrow {}^7F_2$ transitions. This also shows deconvolution using Gaussian fit with offset (dashed lines). Site selective excitation spectra are shown in (b)-(d) with the spectrometer monitoring at 16327, 16090, and 16419 cm^{-1} respectively.

4.1.2 $^5D_0$ Fluorescence

CaF_2:Eu^{3+} nanoparticles have been previously studied spectroscopically. The earliest study known to the author has been done in 2005, published by Wang et al. [6], where fluorescence was observed from the $^5D_0$ multiplet by initially populating ^5L_J electronic states. However this was performed at room temperature. Fluorescence studies on the same materials have been presented in later work by Song et al. [41]. The work by Song et al. modified the surface of the nanoparticles with oleic acid, in order to assist with dispersion in chloroform. This modification has been done with the motivation of making optical components in polymer materials [42]. The two studies also observe different relative intensities of transitions. The study by Wang et al. presented a high $^5D_0 \rightarrow {}^7F_1$ to $^5D_0 \rightarrow {}^7F_2$ transition intensity ratio, indicating that the centre excited has inversion symmetry [43]. By contrast, work by Song et al. shows a stronger $^5D_0 \rightarrow {}^7F_2$ transition, indicating a centre without inversion symmetry. Due to the $^5D_0 \rightarrow {}^7F_1$ transition being magnetic dipole allowed, it is relatively insensitive to effects of the local centre symmetry. This contrasts with the $^5D_0 \rightarrow {}^7F_2$ transition, which is electric dipole allowed and thus is significantly affected by the centre of symmetry around the Eu^{3+} ion.

This study builds on these works by measuring fluorescence originating from the $^5D_0$ multiplet at 10 K at a higher resolution than previously performed. This fluorescence is measured using laser site selective excitation, exciting Eu^{3+} ions in the centres described in Table 4.1. Figures 4.2 to 4.7 show fluorescence from $^5D_0 \rightarrow {}^7F_J$ transitions of Eu^{3+} in these different centres, with transition frequencies and state energies tabulated in Tables 4.2 to 4.4. In each centre studied in this work, the $^5D_0 \rightarrow {}^7F_2$ transition is stronger than the $^5D_0 \rightarrow {}^7F_1$ transition. All of the spectra observed also display heavily broadened spectral lines (with a typical linewidth of > 20 cm^{-1}), due to sample inhomogeneities. All fluorescence was measured at 10 K. A multicomponent Gaussian fit was employed in order to deconvolve individual spectral components associated with different transitions between crystal field levels, with the fit having the same form as that used for deconvolving the broadband excitation spectrum shown in Figure 4.1(a).

Table 4.2 gives the transition energies observed for transitions from the $^5D_0$ multiplet to the ^7F_J multiplets for the centre labelled as site 1, as well as the inferred state energies of the individual crystal field levels. Site 1 was excited at 17249 cm^{-1} and is indicated to be a centre of low symmetry as the $^7F_1$ multiplet displays complete degeneracy lifting. This can be observed in Figure 4.2(a) where three distinct peaks, while broadened, can be identified. Due to this low symmetry centre, all transitions should be observable, which is mostly true for this centre. While the $^5D_0 \rightarrow {}^7F_6$ transition is not visibly present, all other $^5D_0 \rightarrow {}^7F_J$ transitions are observed. No more than (2J+1) crystal field levels are observed in any emission to the ^7F_J multiplets. The energies of the transitions are in the same range as that of both the previous bulk [39, 40] and room temperature nanoparticle [6, 41] studies performed. For the $^5D_0 \rightarrow {}^7F_2$ and $^5D_0 \rightarrow {}^7F_4$ transitions which appear to be phonon sidebands are observed at a reasonable energy for CaF_2 phonons ($\hbar\omega \approx 260$ cm^{-1} [21]).

Table 4.3 gives the transition energies from the observed $^5D_0$ to the ^7F_J multiplets for the centre labelled as site 1a, as well as the state energies of the individual crystal field levels. Site 1a was excited at 17255 cm^{-1} and is also indicated to be a centre of low symmetry due to the $^7F_1$ multiplet's breakdown in degeneracy. This can be observed in Figure 4.3(b),

which displays three distinct peaks, despite overlap from the broadening of the spectral lines. All transitions from $^5D_0$ to ^7F_J are observable, as a result of this lowered symmetry. The energies of these transitions are in the same range as reported in previous works on the bulk [39, 40] and nanoparticles at room temperature [6, 41]. Like site 1, phonon sidebands are observed for $^5D_0 \rightarrow {}^7F_2$ and $^5D_0 \rightarrow {}^7F_4$ transitions.

Table 4.4 gives the transition energies from the observed $^5D_0$ to the ^7F_J multiplets when exciting the centre labelled as site 2. Site 2 was excited at 17274 cm^{-1} and displays a low symmetry, with a broken degeneracy of the $^7F_1$ multiplet. This multiplet also displays more than (2J+1) crystal field levels. However, the excitation of site 2 is not truly site selective, as explained in the previous section and seen in Figure 4.1(d) and is the likely cause of the multiple crystal field levels observed and transitions are present that are not purely a result of exciting site 2. Due to this lack of site selectivity transitions that are unique to site 2 were very difficult to identify. $^5D_0 \rightarrow {}^7F_5$ and $^5D_0 \rightarrow {}^7F_6$ transitions are not observed for this centre. The energies of the transitions observed are in the same range as previous works on the bulk [39, 40] and nanoparticles at room temperature [6, 41]. Like the two previous centres, the $^5D_0 \rightarrow {}^7F_2$ and $^5D_0 \rightarrow {}^7F_4$ transitions display what appear to be phonon sidebands, which have a larger presence in comparison to sites 1 and 1a.

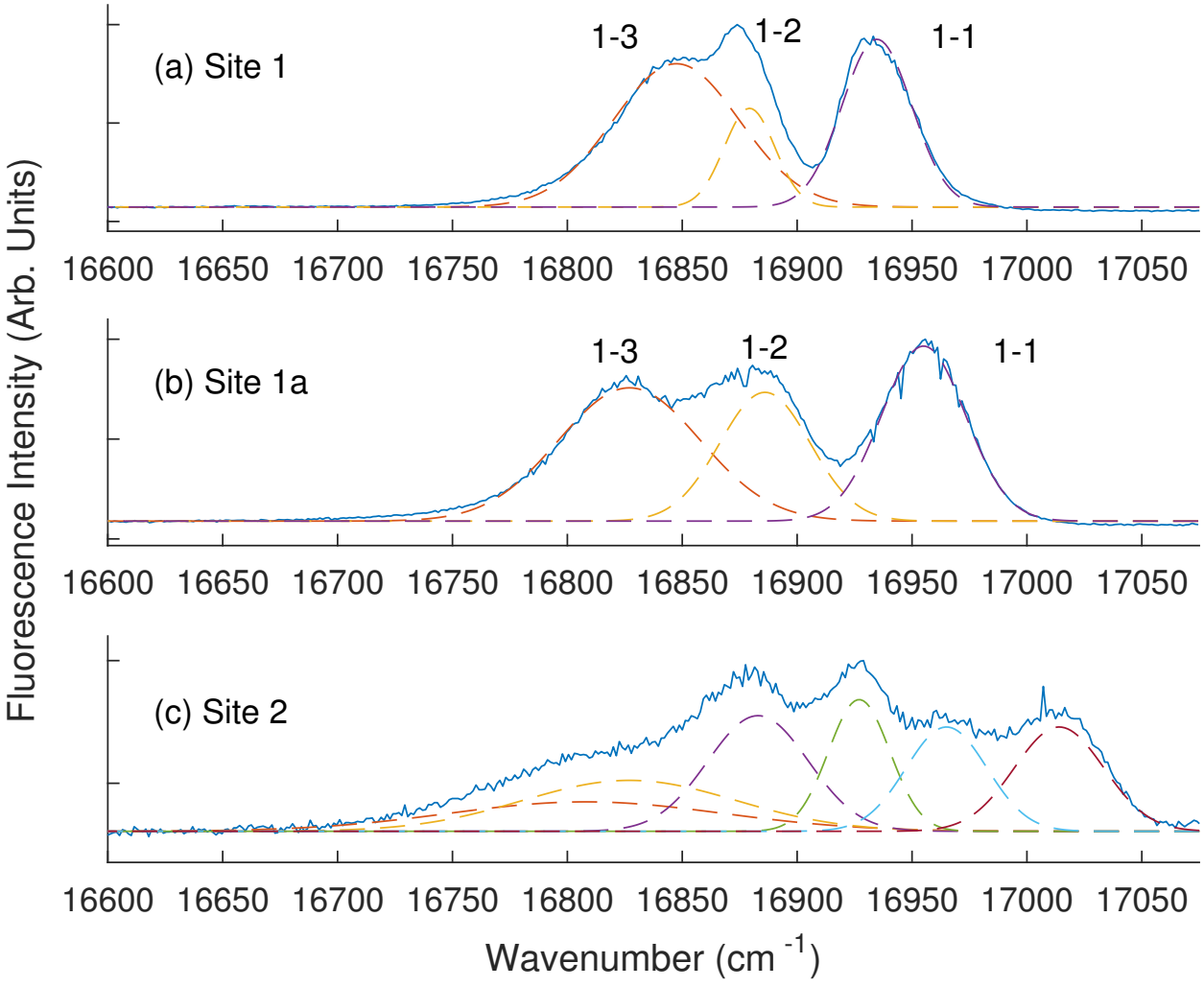

Figure 4.2: 10 K emission to the $^7F_1$ multiplet for the three spectroscopic centres observed.

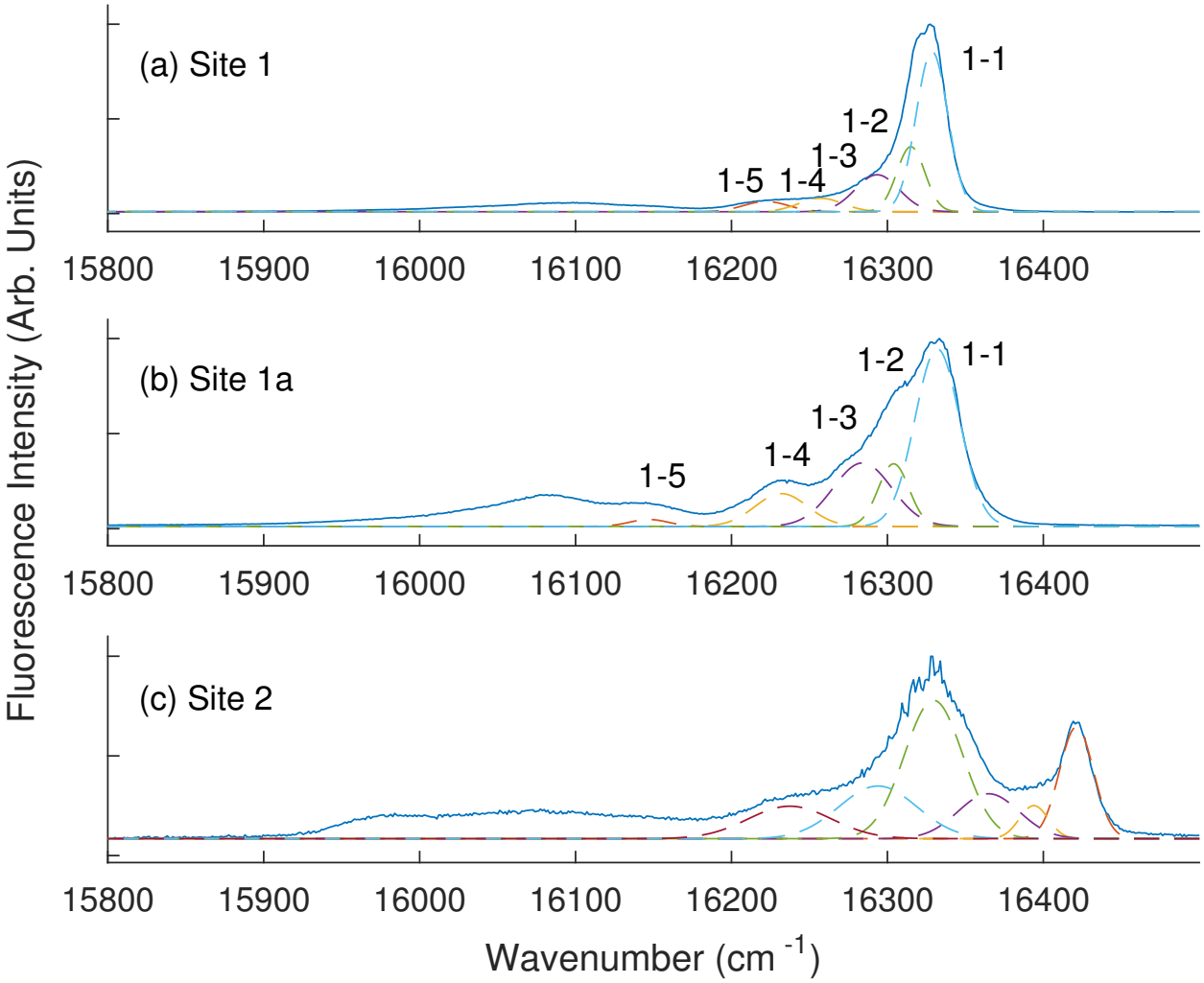

Figure 4.3: 10 K emission to the $^7F_2$ multiplet for the three spectroscopic centres observed.

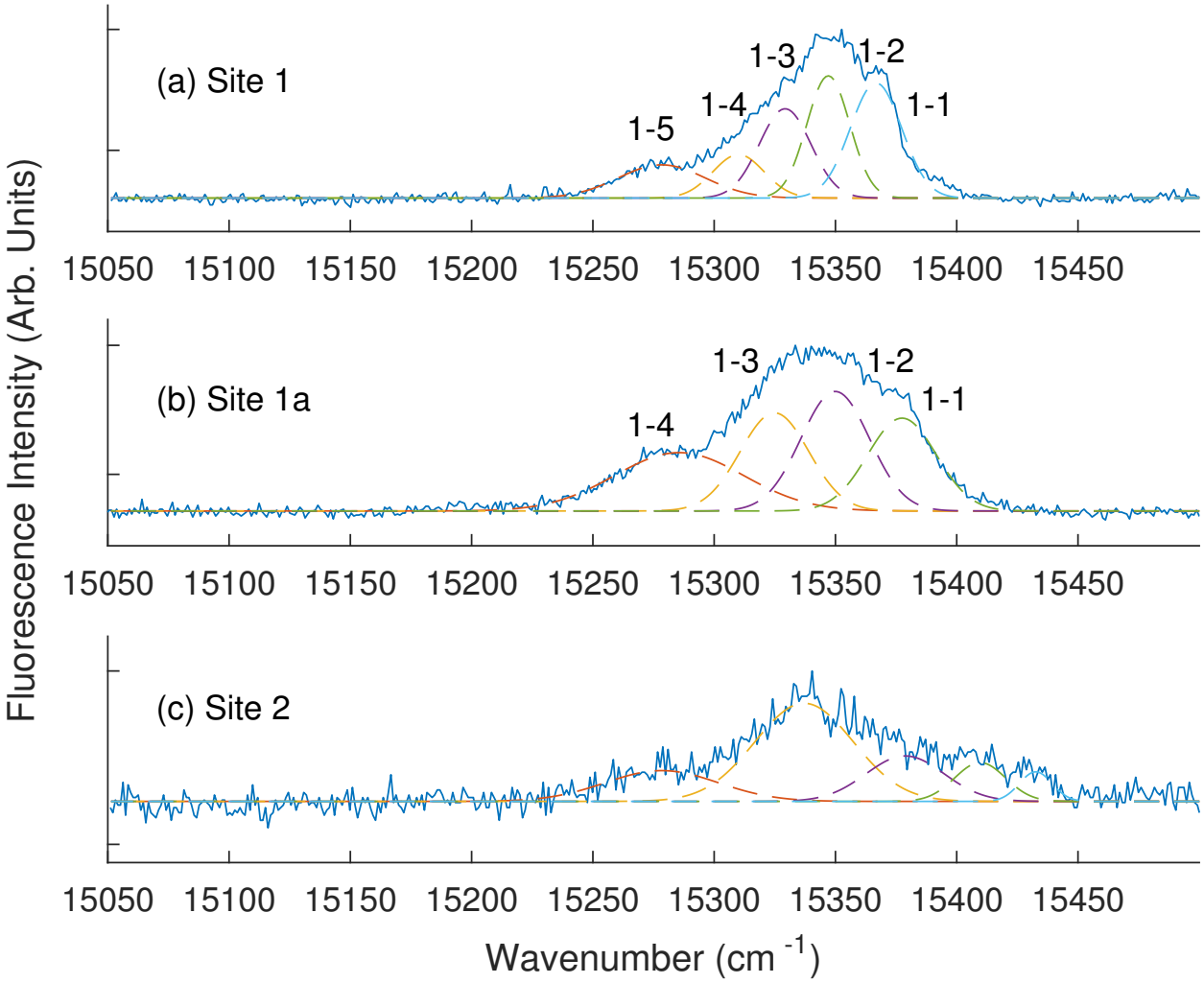

Figure 4.4: 10 K emission to the $^7F_3$ multiplet for the three spectroscopic centres observed.

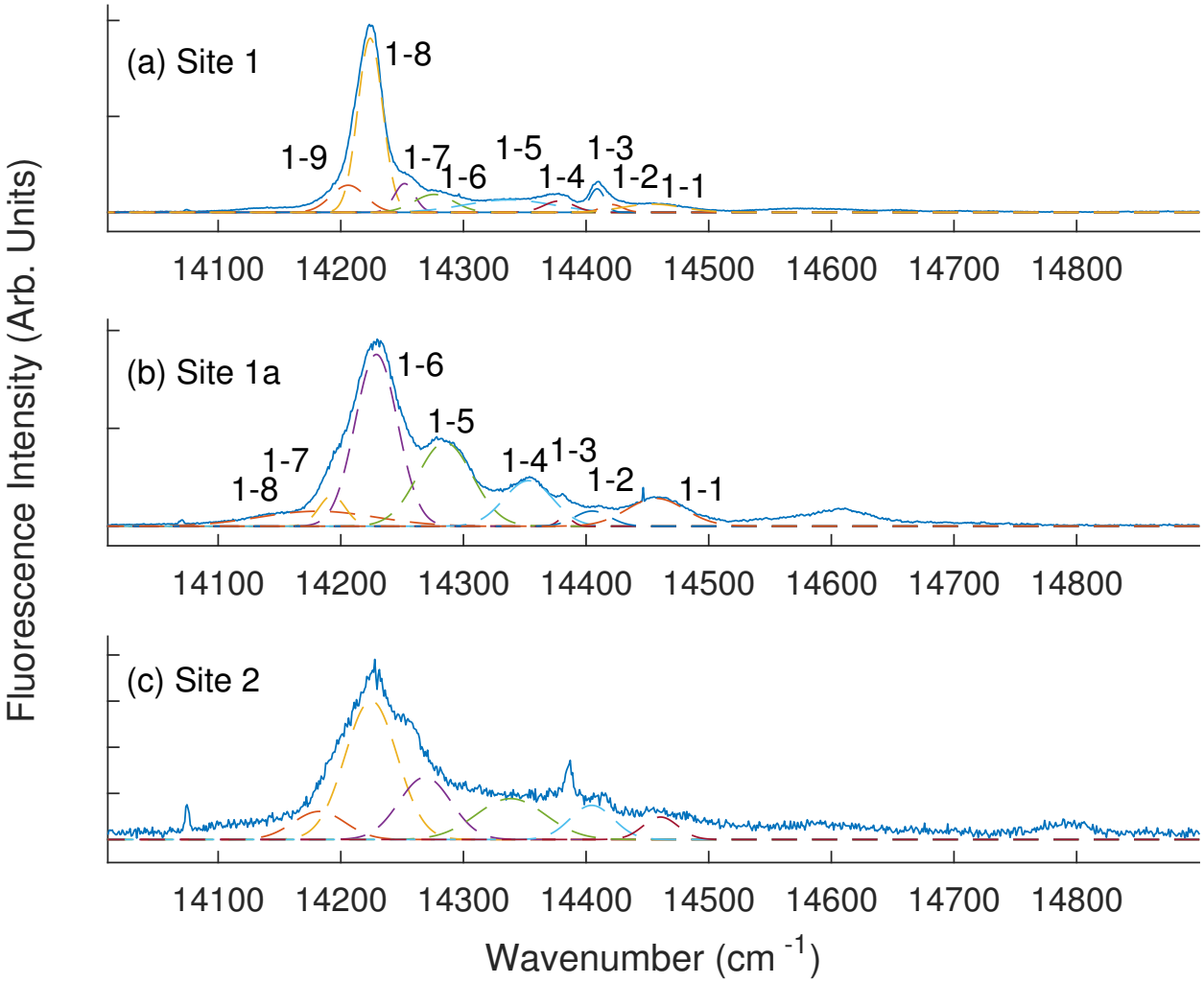

Figure 4.5: 10 K emission to the $^7F_4$ multiplet for the three spectroscopic centres observed.

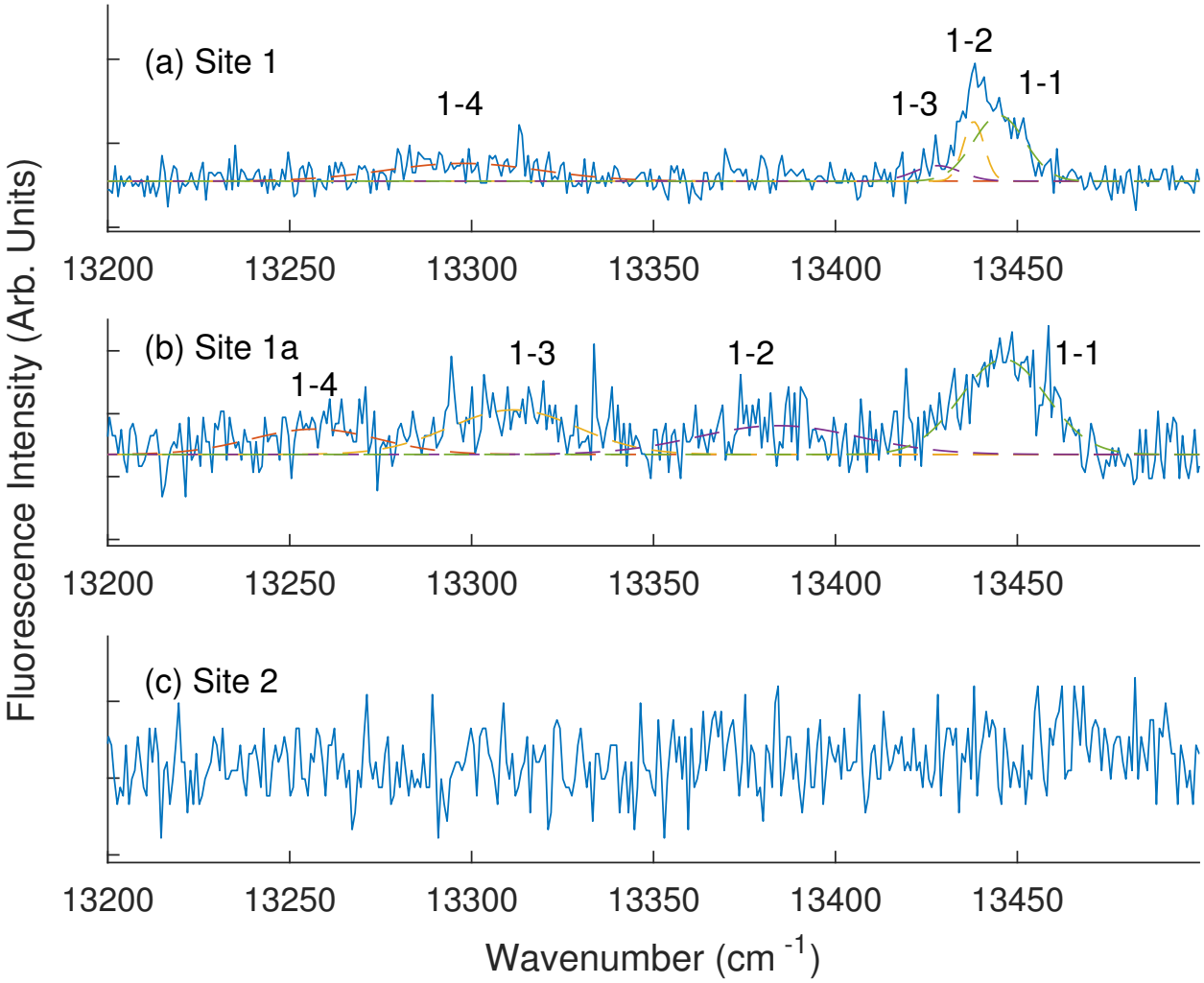

Figure 4.6: 10 K emission to the $^7F_5$ multiplet for the three spectroscopic centres observed.

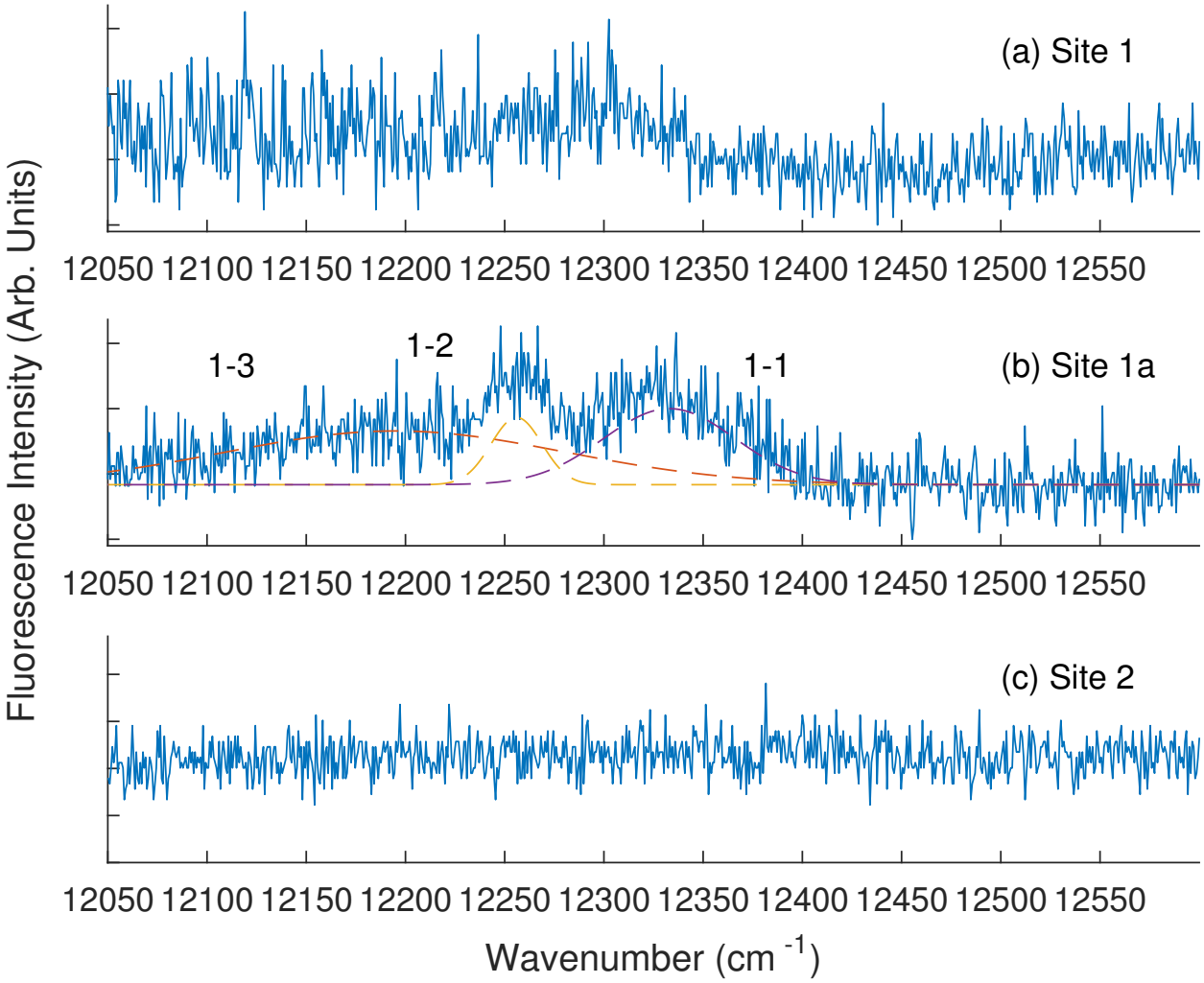

Figure 4.7: 10 K emission to the $^7F_6$ multiplet for the three spectroscopic centres observed.

Table 4.2: Transition frequencies and state energies for site 1 centre in CaF_2:0.25%Eu^{3+} nanoparticles, with transitions originating from the $^5D_1$ multiplet at a laser excitation frequency of 17249 cm^{-1}. The transition frequencies were measured in air (cm^{-1}), with an uncertainty of ± 1 cm^{-1}.

Terminating Multiplet	Transition Frequency	State Energy
$^7F_1$	16935	314
	16879	370
	16847	402
$^7F_2$	16329	920
	16315	934
	16293	954
	16257	992
	16222	1027
$^7F_3$	15367	1882
	15347	1902
	15329	1920
	15310	1939
	15278	1983
$^7F_4$	14454	2795
	14421	2828
	14409	2840
	14378	2871
	14337	2912
	14276	2973
	14252	2997
	14224	3025
	14206	3043
$^7F_5$	13445	3804
	13438	3811
	13428	3821
	13298	3951

Table 4.3: Transition frequencies and state energies for site 1a centre in CaF_2:0.25%Eu^{3+} nanoparticles, with transitions originating from the $^5D_0$ multiplet at a laser excitation frequency of 17255 cm^{-1}. The transition frequencies were measured in air (cm^{-1}), with an uncertainty of ± 1 cm^{-1}.

Terminating Multiplet	Transition Frequency	State Energy
$^7F_1$	16955	300
	16886	369
	16827	428
$^7F_2$	16332	923
	16304	951
	16284	971
	16232	1023
	16147	1108
$^7F_3$	15377	1878
	15350	1905
	15325	1930
	15286	1969
$^7F_4$	14457	2798
	14405	2850
	14383	2872
	14353	2902
	14285	2970
	14229	3026
	14193	3062
	14181	3074
$^7F_5$	13446	3809
	13384	3871
	13311	3944
	13257	3998
$^7F_6$	12333	4922
	12256	4999
	12195	5060

Table 4.4: Transition frequencies of the site 2 centre in CaF_2:0.25%Eu^{3+} nanoparticles, with transitions originating from the $^5D_0$ multiplet at a laser excitation frequency of 17274 cm^{-1}. The transition frequencies were measured in air (cm^{-1}), with an uncertainty of ± 1 cm^{-1}. All fitted electronic transitions are presented, but the lack of true site selectivity shows transitions also observed in sites 1 and 1a.

Terminating Multiplet	Transition Frequency
$^7F_1$	17014
	16965
	16927
	16883
	16827
	16808
$^7F_2$	16421
	16394
	16365
	16330
	16294
	16237
	16093
$^7F_3$	15433
	15410
	15379
	15337
	15278
$^7F_4$	14792
	14588
	14461
	14405
	14339
	14269
	14225
	14182

4.2 $^5D_1$ Excitation and Fluorescence

4.2.1 $^5D_1$ Excitation

Figures 4.8(a) and 4.9(a) show the 10 K fluorescence detected absorption spectra of the CaF_2:0.25%Eu^{3+} nanoparticles. This was obtained by exciting directly to the $^5D_1$ multiplet, monitoring all $^5D_1 \rightarrow {}^7F_4$ and $^5D_0 \rightarrow {}^7F_2$ transitions. The observed spectrum displays heavily broadened spectral lines, due to sample inhomogeneities. As a result, there is a lot of overlap between the spectral lines. Again, a multicomponent Gaussian fit was employed in order to deconvolve individual spectral components associated with distinct spectroscopic centres (this is shown in Figure 4.9(a)).

Figures 4.8(b)-(c) show the 10 K absorption spectra of CaF_2:0.25%Eu^{3+} and the co-doped CaF_2:0.25%Eu^{3+}:2%Na^+ bulk crystals respectively. The nanoparticles studied in this work have been co-doped with sodium in order to increase the crystallinity. Therefore the sodium co-doped bulk crystal has been studied in order to identify the new centres that arise and apply this knowledge to the nanoparticle sample. Eight distinct absorption lines are observed in the bulk CaF_2:Eu^{3+} crystal (see Figure 4.8(b)) and are consistent with that of previous studies [39]. The absorption spectrum observed for the sodium co-doped bulk crystal shows an absence of any cluster lines, as well as a very large reduction in intensity of the lines associated with the $C_{4v}(F^-)$ centre. Figure 4.8(c) shows absorption lines at 19024 and 19033 cm^{-1}, which can be attributed to the $C_{2v}(Na^+)$ centre. The line at 19029 cm^{-1} is the cubic centre absorption peak.

Nine distinct spectral peaks can be observed in the 10 K broadband spectrum of the nanoparticles (shown in Figure 4.9(a)). The observed broadband excitation spectrum shows a very broad feature in same energy range as the cluster absorption lines are observed in the bulk crystal, whereas the larger intensity absorption of the nanoparticles lies closer to the C_{2v} and cubic (O_h) absorption lines of the sodium co-doped bulk sample. Figures 4.9(b)-(e) show the site selective excitation spectra obtained by monitoring fluorescence at 16330, 14229, 16931, and 15396 cm^{-1} respectively. The observed spectra are in reasonable agreement to the fitting of the experimental broadband excitation spectrum, although complete site selectivity has not been obtained. The excitation spectrum for site 2 in Figure 4.9(d) shares structure with the $C_{2v}(Na^+)$ lines in Figure 4.8(c). The two centres focused on in fluorescence studies are sites 1 and 2 because sites 1a and 2a cannot be excited selectively against sites 1 and 2 respectively.

Table 4.5 gives the measured optical frequencies of the $^7F_0 \rightarrow {}^5D_1$ transitions observed in the nanoparticles for each centre. sites 1 and 1a display very similar features and as a result, site selectivity between them is not possible to obtain. sites 2 and 2a, while within the same energy range, have very different structures. The excitation spectrum for site 2a (Figure 4.9(e)) shows a line at approximately 19031 cm^{-1}, which matches up with an excitation frequency for site 2 (Figure 4.9(d)), while its peak for excitation frequency intensity is 19037 cm^{-1}, which is positioned between the first and second excitation frequencies for site 2. The relationship between these sites are very similar to the relative positions of the O_h and C_{2v} centres for the co-doped bulk crystal. Both sites 2 and 2a show broad features in the same range as excitation frequencies are observed for sites 1 and 1a.

Table 4.5: 10 K excitation frequencies for the $^5D_1$ multiplet in CaF_2:0.25%Eu^{3+} nanoparticles. The excitation frequencies were measured in air (cm^{-1}), with an uncertainty of ± 1 cm^{-1}.

Centre	Transition	Optical Frequency (cm^{-1})
Site 1	$Z_1 \rightarrow B_1$	19013
Site 1a	$Z_1 \rightarrow B_1$	19016
Site 2	$Z_1 \rightarrow B_1$	19031
	$Z_1 \rightarrow B_2$	19040
	$Z_1 \rightarrow B_3$	19045
Site 2a	$Z_1 \rightarrow B_1$	19037

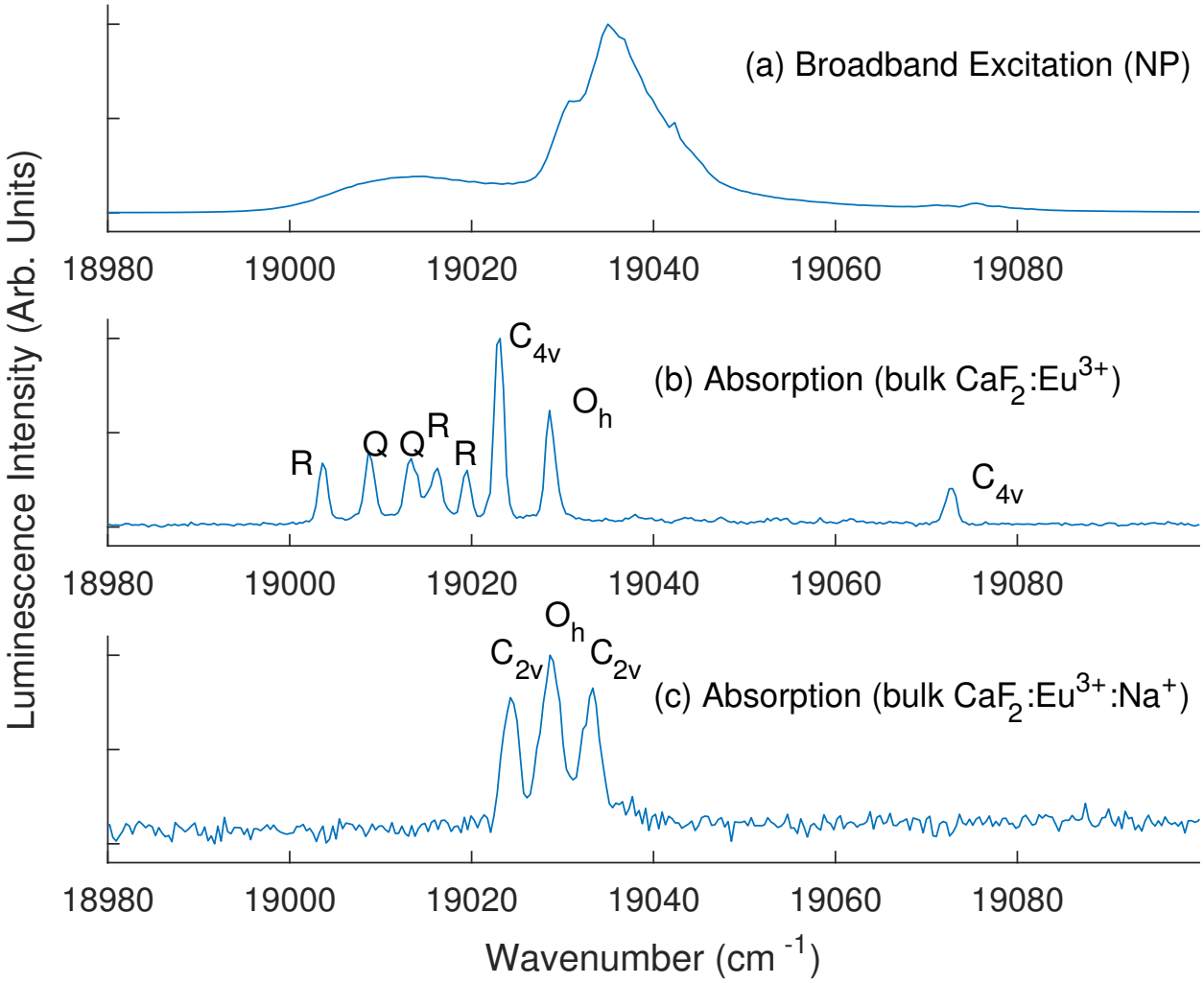

Figure 4.8: (a) 10 K broadband excitation of CaF_2:0.25%Eu^{3+} nanoparticles with the spectrometer monitoring all $^5D_0 \rightarrow {}^7F_2$ and $^5D_1 \rightarrow {}^7F_4$ transitions. 10 K absorption spectra shown in (b)-(c) of the bulk CaF_2:0.25%Eu^{3+} and bulk CaF_2:0.25%Eu^{3+}:2%Na^+ respectively.

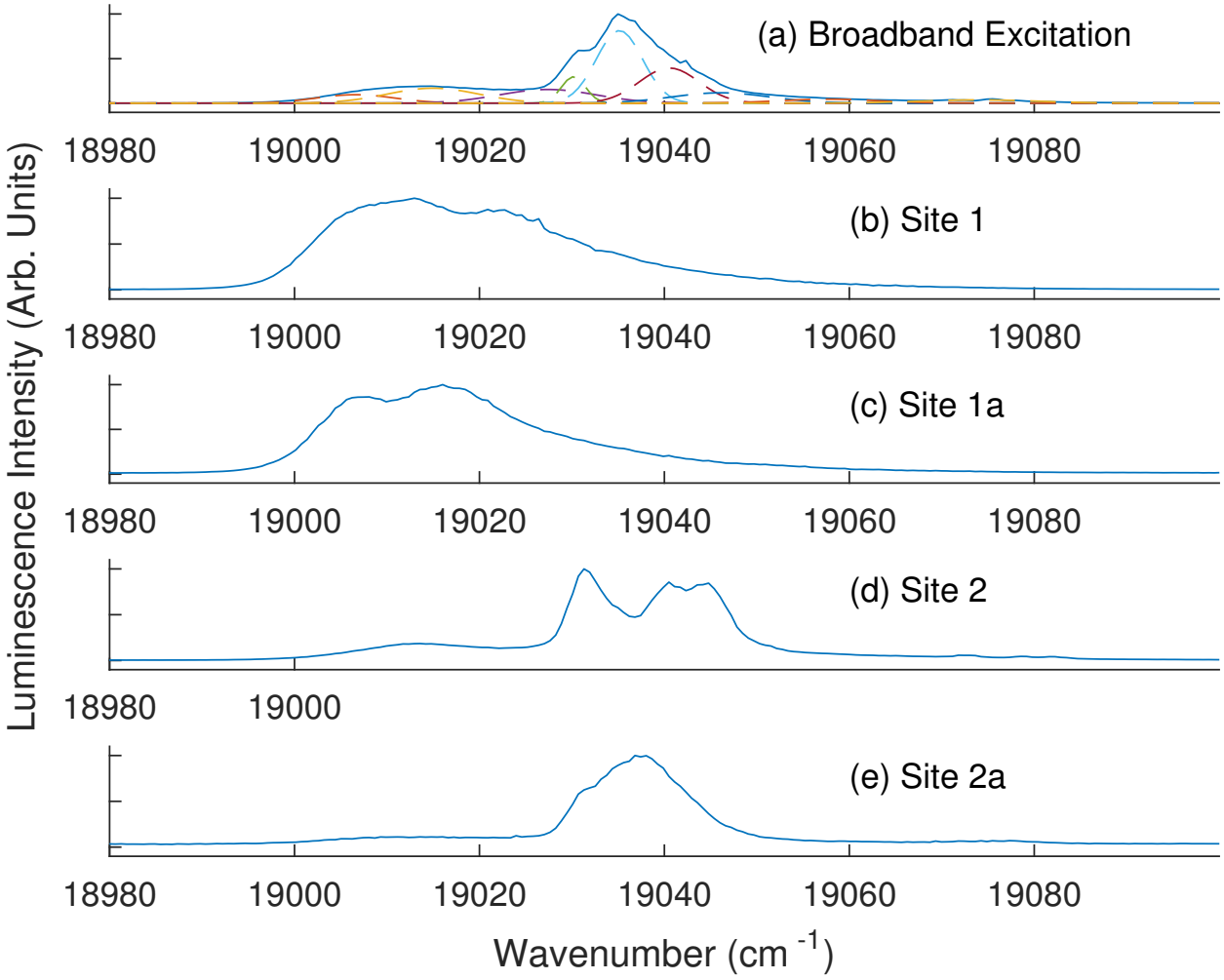

Figure 4.9: (a) 10 K broadband excitation of CaF_2:0.25%Eu^{3+} nanoparticles with the spectrometer monitoring all $^5D_1 \rightarrow {}^7F_4$ transitions. This also shows deconvolution using Gaussian fit with offset (dashed lines). Site selective excitation spectra are shown in (b)-(e) with the spectrometer monitoring at 16330, 14229, 16931, and 15396 cm^{-1} respectively.

4.2.2 $^5D_1$ Fluorescence

The fluorescence from the $^5D_1$ multiplet was measured using site selective excitation, exciting Eu^{3+} ions on selected transitions as given in Table 4.5. Figures 4.10 and 4.11 show fluorescence associated with site 1, whereas Figures 4.12 and 4.13 show fluorescence associated with site 2. All fluorescence was measured at 10 K and the observed spectra show heavily broadened spectral lines, due to sample inhomogeneities. A multicomponent Gaussian fit was employed again in order to deconvolute individual spectral components associated with crystal field levels.

Figure 4.10(a) shows the only observable emission for site 1/1a which lies at frequencies above the $^5D_0 \rightarrow {}^7F_0$ transition. This emission cannot be correlated with $^5D_1 \rightarrow {}^7F_J$ transitions and remains unassigned. All other spectra are comparable to fluorescence from directly exciting to the $^5D_0$ multiplet in sites 1 and 1a. This shows that there must be an extremely fast rate of non-radiative decay from the $^5D_1$ multiplet to the $^5D_0$ multiplet in this centre, possibly indicating that the Eu^{3+} ion emitting is situated on the surface of the nanoparticle. The low symmetry of this centre, can be identified by the observation of complete lifting of degeneracy of the $^7F_1$ multiplet, paired with the relatively low intensity of the observed $^5D_0 \rightarrow {}^7F_1$ transitions when compared to the intensity of the $^5D_0 \rightarrow {}^7F_2$ transitions. Due to this lowered symmetry, all $^5D_0 \rightarrow {}^7F_J$ transitions are observed in this centre. The observed spectra were fitted with information tabulated in Table 4.3, as to draw a correlation between sites. This fitting is in reasonable agreement with the observed spectra. Figures 4.10 and 4.11 show the transitions from the $^5D_0$ multiplet to the $^7F_1$, $^7F_2$, $^7F_3$, $^7F_4$ $^7F_5$, and $^7F_6$ multiplets respectively. These observed transitions are in the range of previous work done on the bulk crystal [39, 40] and previous studies on nanoparticles performed [6, 41], and agree with previous observations in this work. The spectra obtained exciting at 19013 cm^{-1} yield $^5D_0$ emission which is directly correlated with the emission for sites 1/1a when $^5D_0$ itself is directly excited at 17249 or 17255 cm^{-1}. As is evident from the excitation spectra, it is not possible to be site selective for sites 1/1a.

Figures 4.12 and 4.13 show the observed transitions after exciting site 2 at 19045 cm^{-1}. As the $^5D_1$ multiplet is initially populated at 19045 cm^{-1}, intra-multiplet non-radiative relaxation causes emission from the $^5D_1$ state at 19031 cm^{-1}. Unique features are observed in Figures 4.12(a) and (b) and are assigned as $^5D_1 \rightarrow {}^7F_1$ and $^5D_1 \rightarrow {}^7F_2$ transitions respectively (see Table 4.6). The $^5D_1 \rightarrow {}^7F_1$ transition observed at 16869 cm^{-1} places the inferred state energy at 342 cm^{-1}, which is very close to a transition observed in site 2 fluorescence from direct $^5D_0$ excitation. Another peak can be observed at 18347 cm^{-1} and appears to be a phonon, due to its transition energy not being within the range of energies for either a transition to the $^7F_1$ or $^7F_2$ multiplets.

In Figure 4.12(c), the $^5D_0 \rightarrow {}^7F_0$ transition can be observed at 17257 cm^{-1} with a shoulder observed at 17274 cm^{-1}. This observation is consistent with the overall lack of site selectivity obtained throughout this work. Thus $^5D_0$ emission is generated for not only site 2 but site 1/1a as well. Thus transitions are observed that correlate with direct excitation of $^5D_0$ for site 2, mixed in amongst site 1 transitions. Examples of this are the transitions at 17014 and 16421 cm^{-1}, which are labelled as $^5D_0 \rightarrow {}^7F_1$ (see Figure 4.2(c)) and $^5D_0 \rightarrow {}^7F_2$ transitions (see Figure 4.3(c)) respectively.

Table 4.6: Transition frequencies and state energies for site 2 centre in CaF_2:0.25%Eu^{3+} nanoparticles, with transitions originating from the $^5D_1$ multiplet at 19031 cm^{-1}. The transition frequencies were measured in air (cm^{-1}), with an uncertainty of ± 1 cm^{-1}.

Terminating Multiplet	Transition Frequency	State Energy
$^7F_1$	18689	342
$^7F_2$	18224	807
	17866	1165
	17695	1336

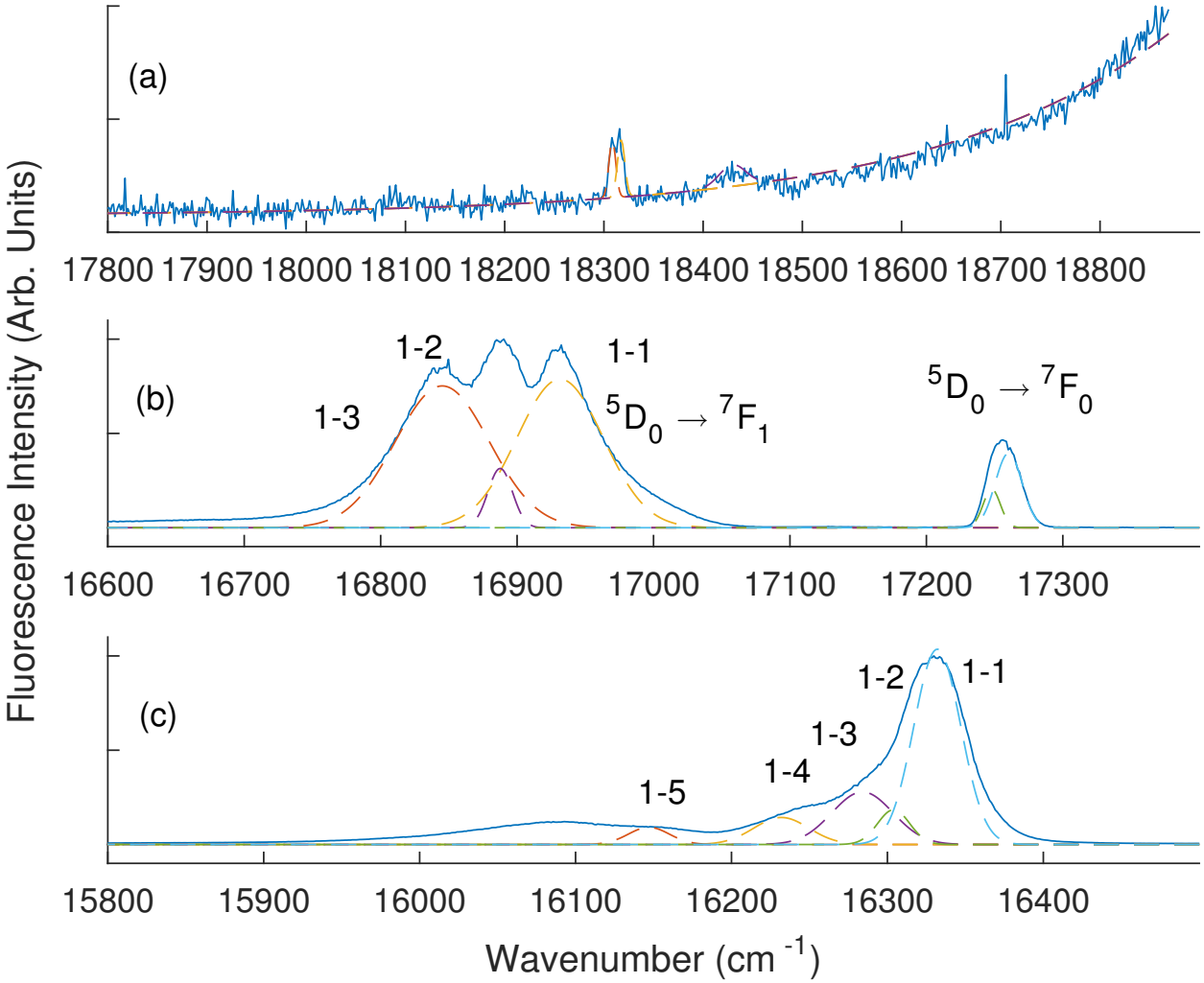

Figure 4.10: 10 K fluorescence of CaF_2:0.25%Eu^{3+} nanoparticles for site 1. (a) shows an unassigned emission. (b) shows both $^5D_0 \rightarrow {}^7F_0$ and $^5D_0 \rightarrow {}^7F_1$ transitions and (c) shows $^5D_0 \rightarrow {}^7F_2$ transitions.

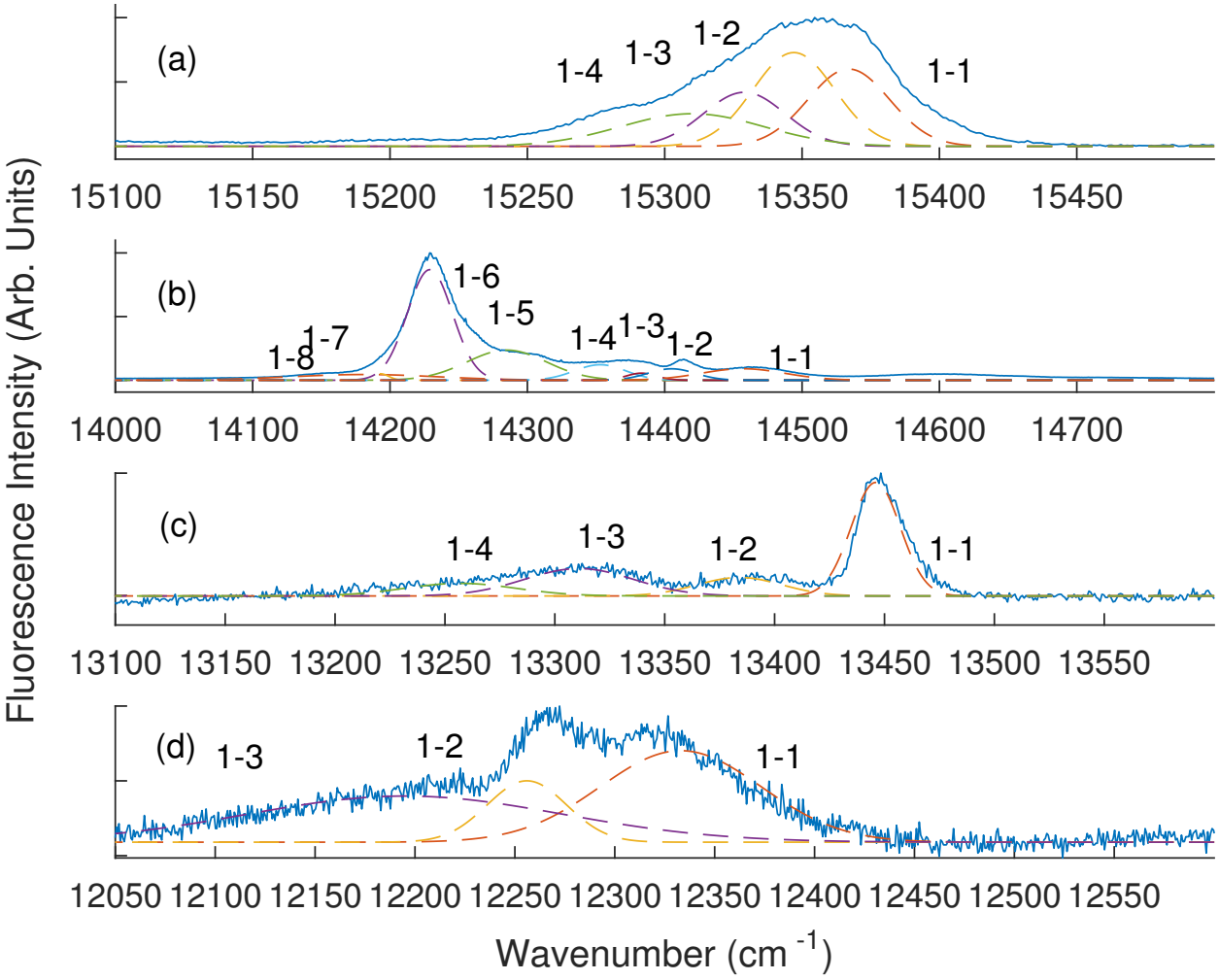

Figure 4.11: 10 K fluorescence of CaF_2:0.25%Eu^{3+} nanoparticles for site 1. (a) shows emission from the $^5D_0$ multiplet to $^7F_3$. (b) shows $^5D_0 \rightarrow {}^7F_4$ transitions. (c) shows $^5D_0 \rightarrow {}^7F_5$ transitions and (d) shows $^5D_0 \rightarrow {}^7F_6$ transitions.

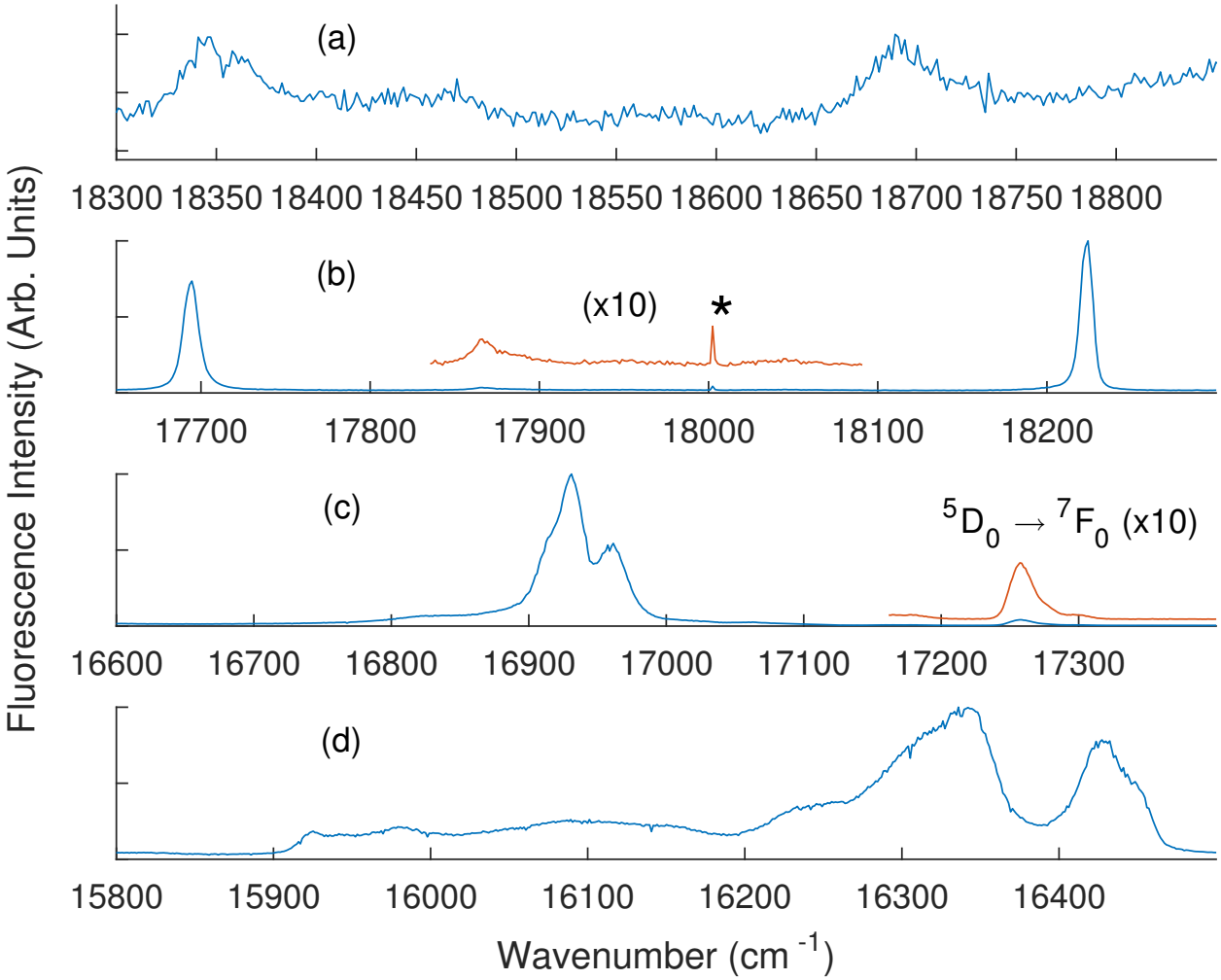

Figure 4.12: 10 K fluorescence of CaF_2:0.25%Eu^{3+} nanoparticles for site 2, excited at 19045 cm^{-1}. (a) shows a $^5D_1 \rightarrow {}^7F_1$ transition and (b) shows $^5D_1 \rightarrow {}^7F_2$ transitions. (c) and (d) show $^5D_0 \rightarrow {}^7F_1$ and $^5D_0 \rightarrow {}^7F_2$ transitions, respectively. Transitions to the $^7F_3$ and $^7F_4$ multiplets from the $^5D_1$ multiplet are also mixed into the spectra for (c) and (d) respectively. The asterisk denotes an artifact.

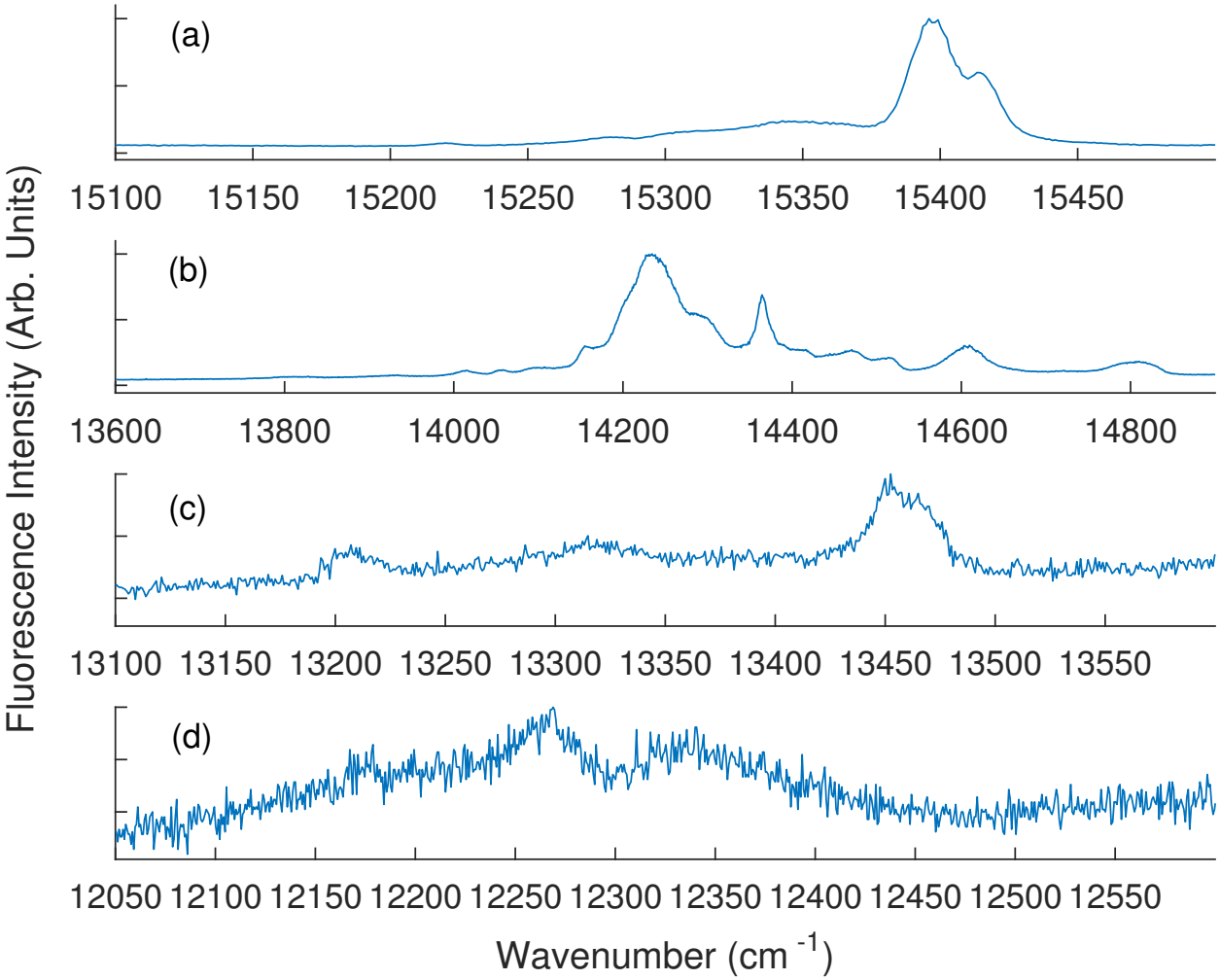

Figure 4.13: 10 K fluorescence of CaF_2:0.25%Eu^{3+} nanoparticles for site 2, excited at 19045 cm^{-1}. (a)-(d) shows transitions from the $^5D_0$ multiplet to $^7F_3$, $^7F_4$, $^7F_5$, and $^7F_6$ multiplets respectively. Transitions to the $^7F_5$ and $^7F_6$ multiplets from the $^5D_1$ multiplet are mixed into the spectra in (a) and (b) respectively, with (c) and (d) showing transitions from the $^5D_0$ multiplets to the $^7F_5$ and $^7F_6$ multiplets respectively as observed in sites 1/1a.

4.3 Fluorescence Lifetimes

The fluorescence decay of sites 1, 1a, and 2 have been measured for the CaF_2:Eu^{3+} nanoparticles, cooled to 10 K. The $^5D_0$ and $^5D_1$ multiplets were studied and results are shown in Table 4.7; with the observed decay curves are shown in Figures 4.14 and 4.15. No lifetime data for the $^5D_1$ multiplet in sites 1/1a could be measured due to the extremely fast relaxation time into the $^5D_0$ multiplet, nor was any risetime observable for excitation of their $^5D_1$ levels when monitoring $^5D_0$ emission.

Lifetimes for the $^5D_0$ multiplet were measured twice. Firstly, the $^5D_0$ multiplet was directly excited, using Rhodamine 6G dye. Secondly, the $^5D_1$ multiplet was excited directly using Coumarin 500 dye and non-radiative relaxation from this multiplet allowed population of the $^5D_0$ multiplet. The lifetimes of the $^5D_0$ multiplets in sites 1/1a and 2 have been measured to be 2.5 and 3.7 ms respectively, which is very low when compared to previous work done on the bulk. In the bulk crystal, the lifetime of the $^5D_0$ multiplet in the C_{4v} centre was measured as 11.8 ms. The larger lifetime in the bulk reflects its position inside the lattice and the lack of non-radiative relaxation from $^5D_0$. The reduction in lifetime in the case of the nanoparticles suggest a completely different configuration. The $^5D_1$ multiplet lifetime measured in site 2 is less than that of the bulk, but within the same magnitude (multiple milliseconds). This can possibly be attributed to the change of phonon density of states between the bulk and the nanoparticle, where it becomes discretised in the nanoparticle.

Table 4.7: 10 K fluorescence lifetimes (in ms) for the $^5D_0$ and $^5D_1$ multiplets in sites 1/1a and 2/2a in CaF_2:Eu^{3+} nanoparticles.

Centre	Multiplet	Nanoparticle Lifetime	Bulk Crystal Lifetime
Site 1/1a	$^5D_0$	2.5 ± 0.1	11.8 (C_{4v}) [39]
Site 2	$^5D_0$	3.7 ± 0.2	11.8 (C_{4v}) [39]
	$^5D_1$	2.4 ± 0.1	3.6 (C_{4v}) [39]
Site 2a	$^5D_0$	17.4 ± 0.1	24 (O_h) [25]
	$^5D_1$	2.7 ± 0.1	3.6 (O_h) [25]

The $^5D_0 \rightarrow {}^7F_1$ transition at 16927 cm^{-1} was also monitored and this decay curve is shown in Figure 4.16. The lifetime of 17.4 ms measured for this transition line is very different to all other lifetimes measured in either centres in that it reflects the same characteristic as the bulk sample, indicating a position inside the lattice. The rise time (2.7 ms) before decay shows that the population is not a result of direct laser excitation, but instead it is a result of decay into the $^5D_0$ multiplet from the $^5D_1$ multiplet. We speculate that this may arise from site 2a emission which looks close to cubic and is necessarily excited when pumping site 2. We note that the cubic centre $^5D_0$ lifetime in bulk CaF_2 crystals is 24 ms at 15 K [25].

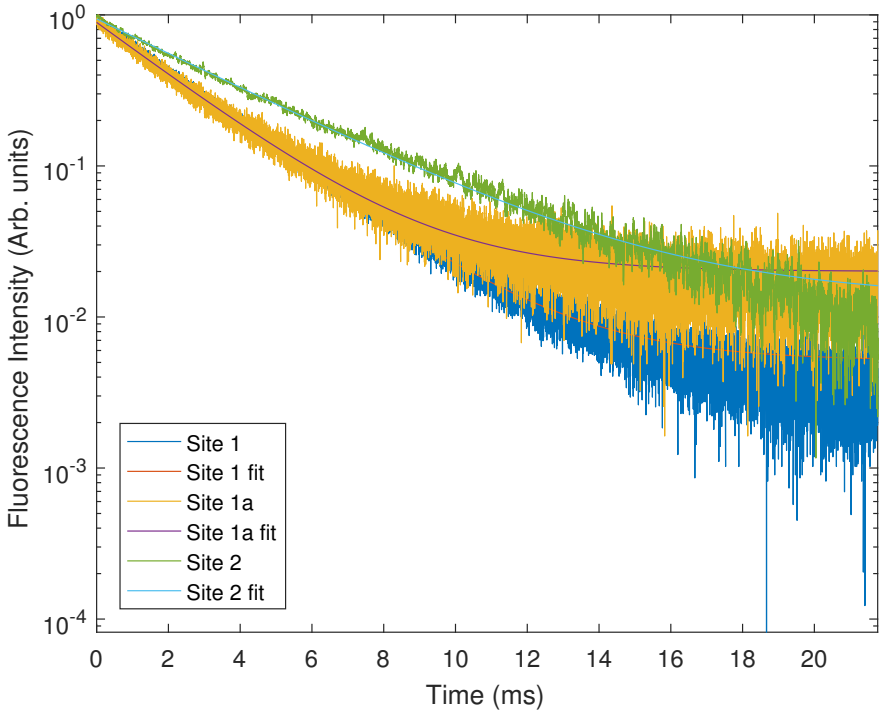

Figure 4.14: 10 K fluorescence decay monitoring sites 1, 1a, and 2 after excitation to the $^5D_0$ multiplet. The transitions monitored are $^5D_0 \rightarrow {}^7F_2$ transitions at 16329, 16090, and 16421 cm^{-1} respectively.

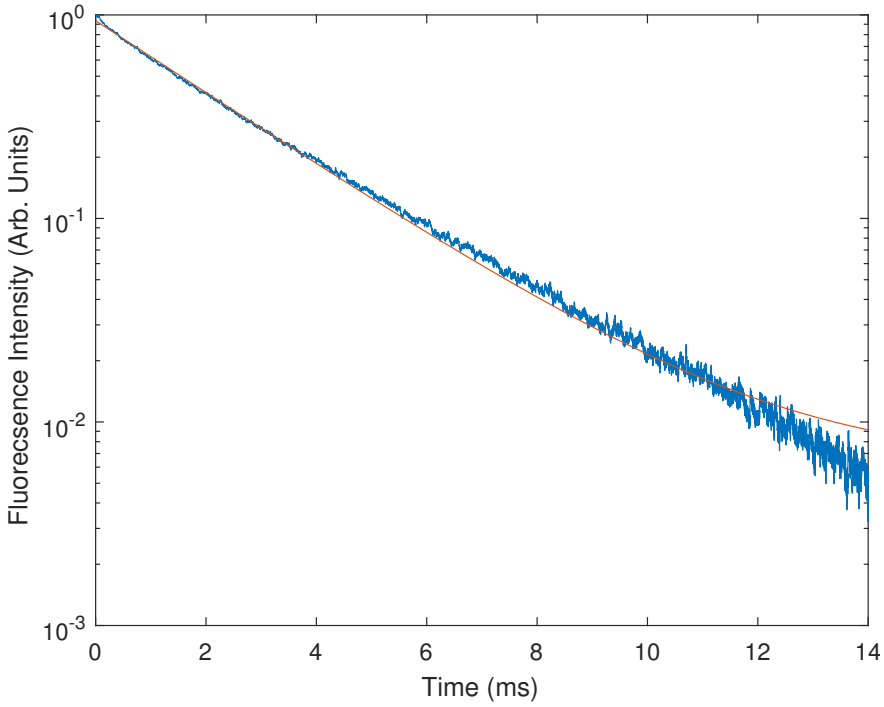

Figure 4.15: 10 K fluorescence decay monitoring site 2, specifically, the $^5D_1 \rightarrow {}^7F_2$ transition at 18224 cm^{-1}.

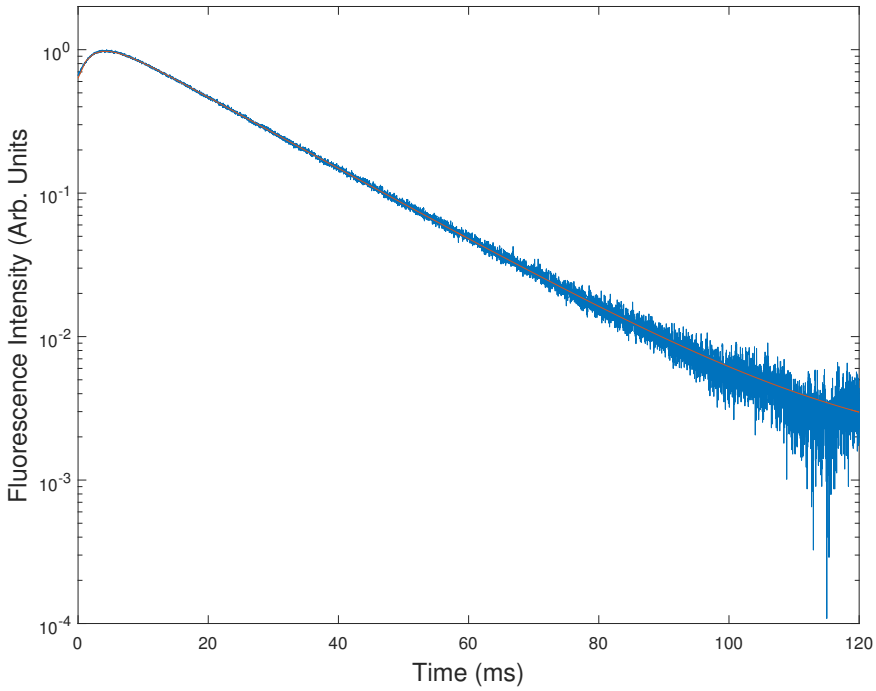

Figure 4.16: 10 K $^5D_0$ fluorescence decay monitoring site 2a (tentative assignment), specifically, the $^5D_0 \rightarrow {}^7F_1$ transition at 16927 cm^{-1}.

Chapter 5

Conclusions

This study has utilised laser selective excitation and fluorescence of CaF_2:0.25%Eu^{3+} nanoparticles, each with a diameter of <10 nm. Four distinct spectroscopic centres have been identified and studied, with fluorescence lifetimes having been determined for at least three of these centres. Where possible, the spectroscopy performed here has been compared to the analogous bulk crystal samples.

Laser site selective spectroscopy has been employed to excite the Eu^{3+} ion from its $^7F_0$ ground state to both the $^5D_0$ and $^5D_1$ multiplets. In direct excitation to $^5D_0$, three distinct centres were observed and in direct excitation to $^5D_1$, four distinct centres were observed. Fluorescence studies have allowed us to correlate excitation features observed for both the $^5D_0$ and $^5D_1$ multiplets. The centres labelled site 1/1a show no detectable $^5D_1$ fluorescence. This indicates fast non-radiative relaxation from $^5D_1$ to $^5D_0$. The lifetime of the $^5D_0$ multiplet in this centre has been measured to be 2.5 ms. This value is short when compared to centres in the bulk crystal counterpart. This, as well as an observed low symmetry, leads us to propose that sites 1 and 1a are surface sites. The similarity between the spectroscopic structures of these sites suggests a bimodal distribution of ions residing on, or near, the surface of the nanoparticle.

The centre labelled site 2 shows emission from the $^5D_1$ multiplet and the strongest and the most recognisable of these are transitions to $^7F_2$, with this fluorescence having a lifetime of 2.4 ms, which is not significantly different to the $^5D_1$ multiplet lifetime measured in the bulk crystal (3.6 ms [39]). When measuring lifetimes for the $^5D_0$ multiplet of this site, the transition to $^7F_2$ gave a lifetime of 3.7 ms in both direct excitation to $^5D_0$ and $^5D_1$. An additional centre, which we label here as 'site 2a' has an excitation feature which spectrally overlaps that for site 2, for the $^5D_1$ multiplet. It is notable that when monitoring selected $^5D_0 \rightarrow {}^7F_1$ transition features a very long lifetime of 17.4 ms can be observed, having a rise time of 2.7 ms. This emission appears to be correlated with site 2a and its long lifetime is very similar to that measured for cubic centres in the bulk crystal. This may also explain the absence of $^5D_0$ excitation features for this centre. We further note the close similarities between site 2 and the $C_{2v}(Na^+)$ centre of the bulk crystal and tentatively conclude that both site 2 and 2a are centres inside the nanoparticle.

Future work will be important in further determining the nature of the centres observed and presented in this thesis. Site 2a has not been heavily studied in this work, although the fluorescence detected absorption shows this centre to be the strongest in intensity. Further

study of this centre will allow one to confirm the tentative conclusions drawn about the centre in this work (or conclude differently).

In order to clarify whether or not sites 1 and 1a are surface sites, nanoparticles of the same core can be grown with a coating of undoped CaF_2. This will extinguish the fluorescence observed from any surface sites and any resultant centres can be correlated to the work presented in this thesis. From the measurements made here it is not possible to identify cluster centres (which would be desirable for bio-medical imaging). One possibility is to prepare CaF_2:Eu^{3+} nanoparticles co-doped with Sm^{3+}, and having an inert shell placed around them. In that case any cluster centres present will be identifiable since optical pumping of the $^4G_{5/2}$ multiplet of the Sm^{3+} should lead to the $^5D_0$ emission of Eu^{3+} through inter-ionic energy transfer. Sm^{3+} only clusters will not emit visibly since the optical excitation of $^4G_{5/2}$ will be quenched by cross relaxation.

Appendix A

Appendix

A.1 LabVIEW Data Acquisition Program

This section shows the LabVIEW program used to acquire data from laser site selective excitation and fluorescence experiments. The program operates the same in each case, with the laser and spectrometer being stepped in excitation and fluorescence experiments respectively. This program has been extensively modified by the author for the purposes of this work, although the core program had already been created and all sub VI's were supplied by the equipment manufacturers.

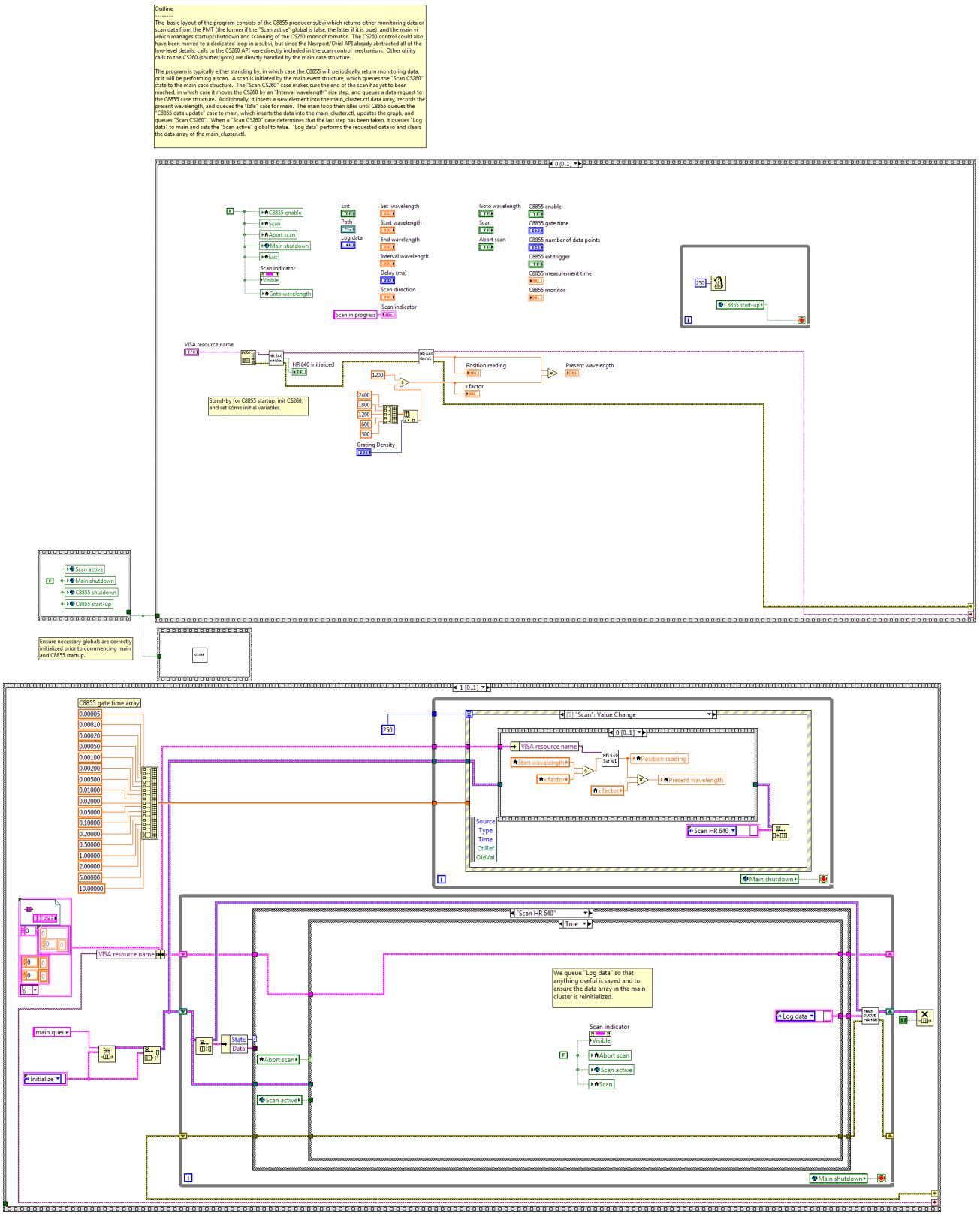
Outline
The basic layout of the program consists of the C8855 producer subvi which returns either monitoring data or scan data from the PMT (the former if the "Scan active" global is false, the latter if it is true), and the main vi which manages startup/shutdown and scanning of the CS260 monochromator. The CS260 control could also have been moved to a dedicated loop in a subvi, but since the Newport/Oriel API already abstracted all of the low-level details, calls to the CS260 API were directly included in the scan control mechanism. Other utility calls to the CS260 (shutter/goto) are directly handled by the main case structure.
The program is typically either standing by, in which case the C8855 will periodically return monitoring data, or it will be performing a scan. A scan is initiated by the main event structure, which queues the "Scan CS260" state to the main case structure. The "Scan CS260" case makes sure the end of the scan has yet to been reached, in which case it moves the CS260 by an "Interval wavelength" size step, and queues a data request to the C8855 case structure. Additionally, it inserts a new element into the main_cluster.ctl data array, records the present wavelength, and queues the "Idle" case for main. The main loop then idles until C8855 queues the "C8855 data update" case to main, which inserts the data into the main_cluster.ctl, updates the graph, and queues "Scan CS260". When a "Scan CS260" case determines that the last step has been taken, it queues "Log data" to main and sets the "Scan active" global to false. "Log data" performs the requested data io and clears the data array of the main_cluster.ctl.
C8855 enable
Scan
Abort scan
Main shutdown
Exit
Scan indicator
Visible
Goto wavelength
Exit
Path
Log data
Set wavelength
Start wavelength
End wavelength
Interval wavelength
Delay (ms)
Scan direction
Scan indicator
Scan in progress
Goto wavelength
Scan
Abort scan
C8855 enable
C8855 gate time
C8855 number of data points
C8855 ext trigger
C8855 measurement time
C8855 monitor
250
C8855 start-up
VISA resource name
HR 640 initialized
Stand-by for C8855 startup, init CS260, and set some initial variables.
1200
Position reading
x factor
Present wavelength
2400
1800
1200
600
300
Grating Density
Scan active
Main shutdown
C8855 shutdown
C8855 start-up
Ensure necessary globals are correctly initialized prior to commencing main and C8855 startup.
C8855 gate time array
0.00005
0.00010
0.00020
0.00050
0.00100
0.00200
0.00500
0.01000
0.02000
0.05000
0.10000
0.20000
0.50000
1.00000
2.00000
5.00000
10.00000
250
[5] "Scan": Value Change
VISA resource name
Start wavelength
x factor
Position reading
Present wavelength
Source
Type
Time
CtlRef
OldVal
Scan HR 640
Main shutdown
"Scan HR 640"
True
VISA resource name
We queue "Log data" so that anything useful is saved and to ensure the data array in the main cluster is reinitialized.
Log data
main queue
Initialize
State
Data
Abort scan
Scan active
Scan indicator
Visible
Abort scan
Scan active
Scan
Main shutdown

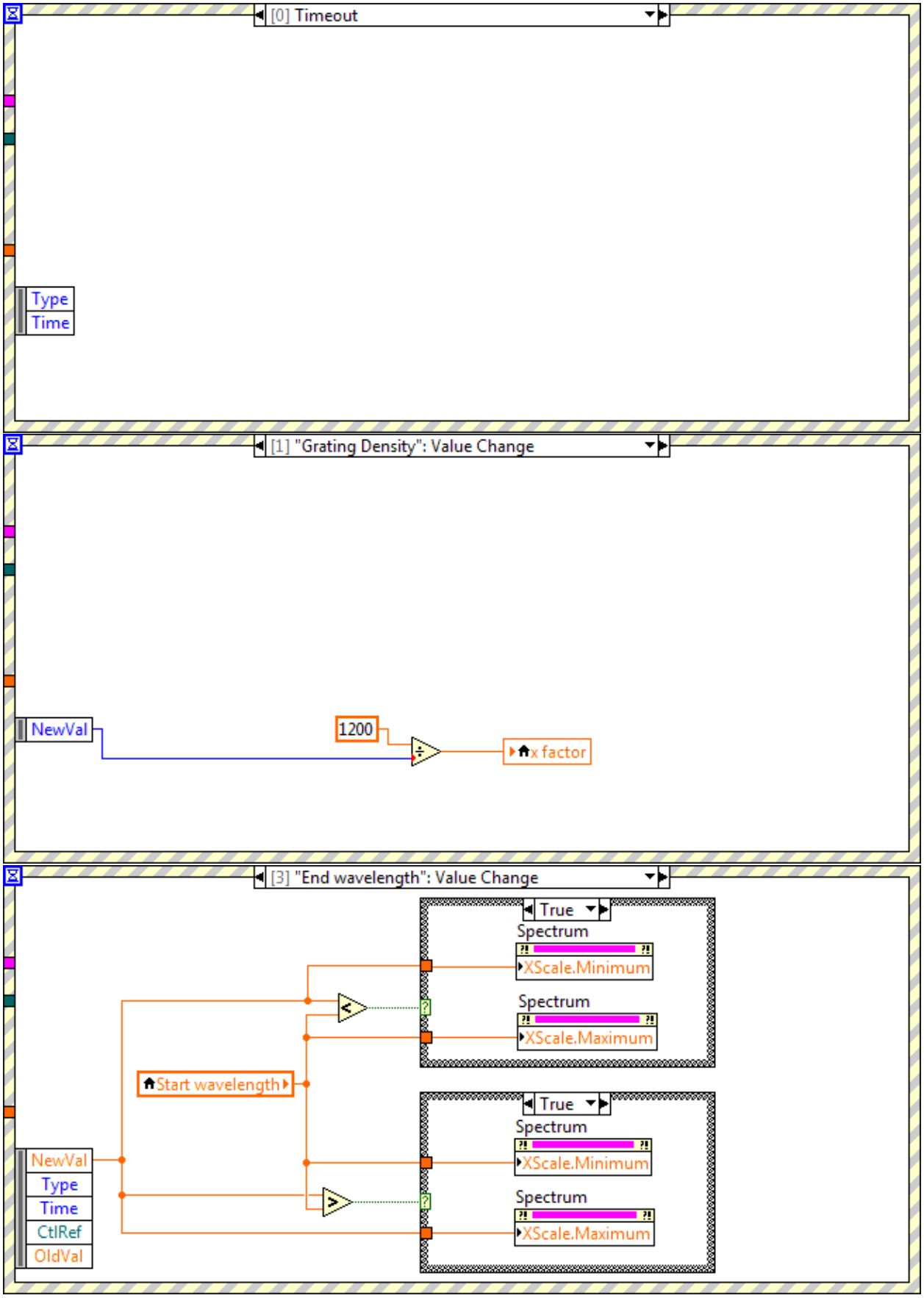
[0] Timeout
Type
Time
[1] "Grating Density": Value Change
NewVal
1200
÷
x factor
[3] "End wavelength": Value Change
True
Spectrum
XScale.Minimum
Spectrum
XScale.Maximum
<
Start wavelength
True
Spectrum
XScale.Minimum
Spectrum
XScale.Maximum
>
NewVal
Type
Time
CtlRef
OldVal

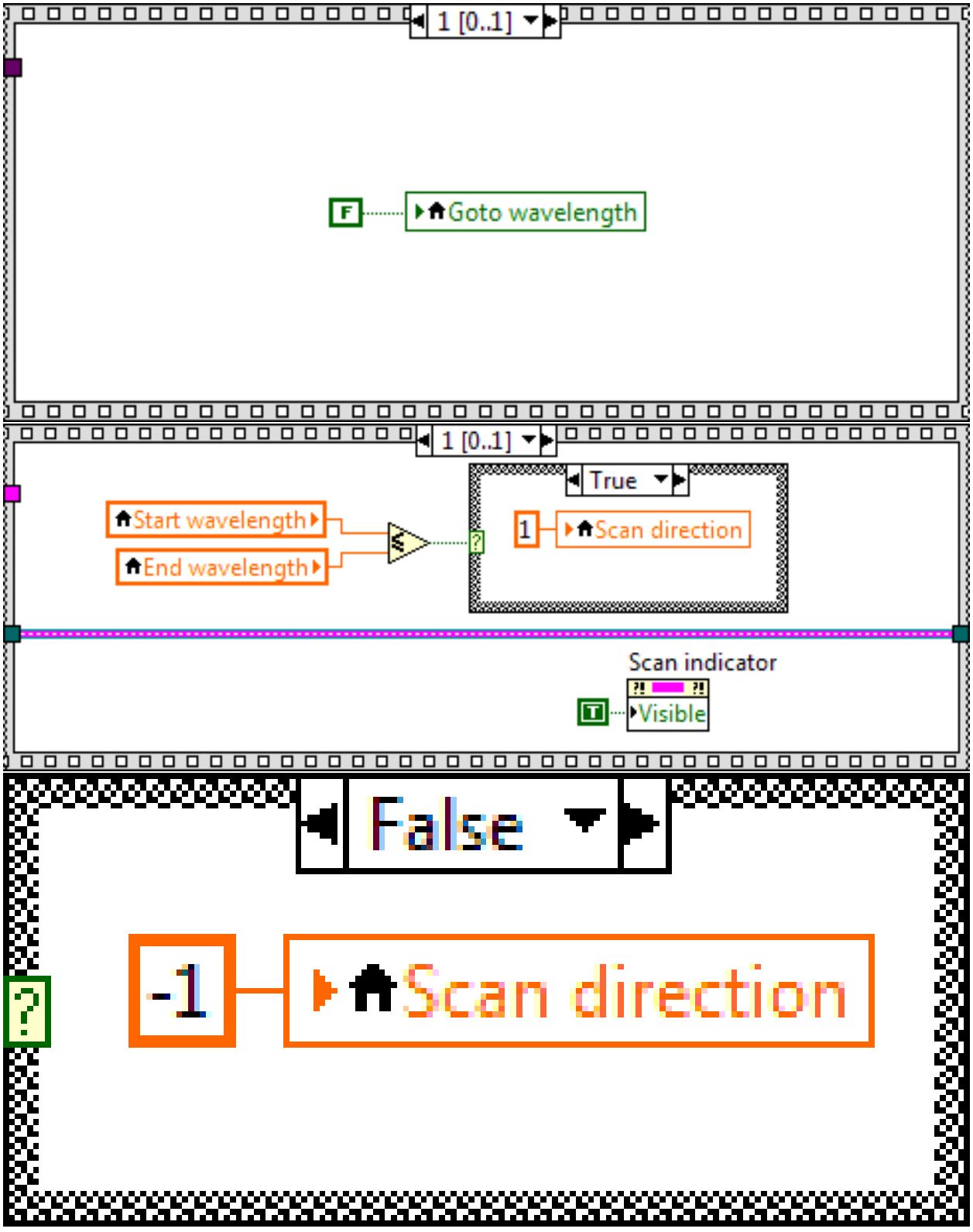
1 [0..1]
F
Goto wavelength
1 [0..1]
True
Start wavelength
End wavelength
1
Scan direction
Scan indicator
T
Visible
False
?
-1
Scan direction

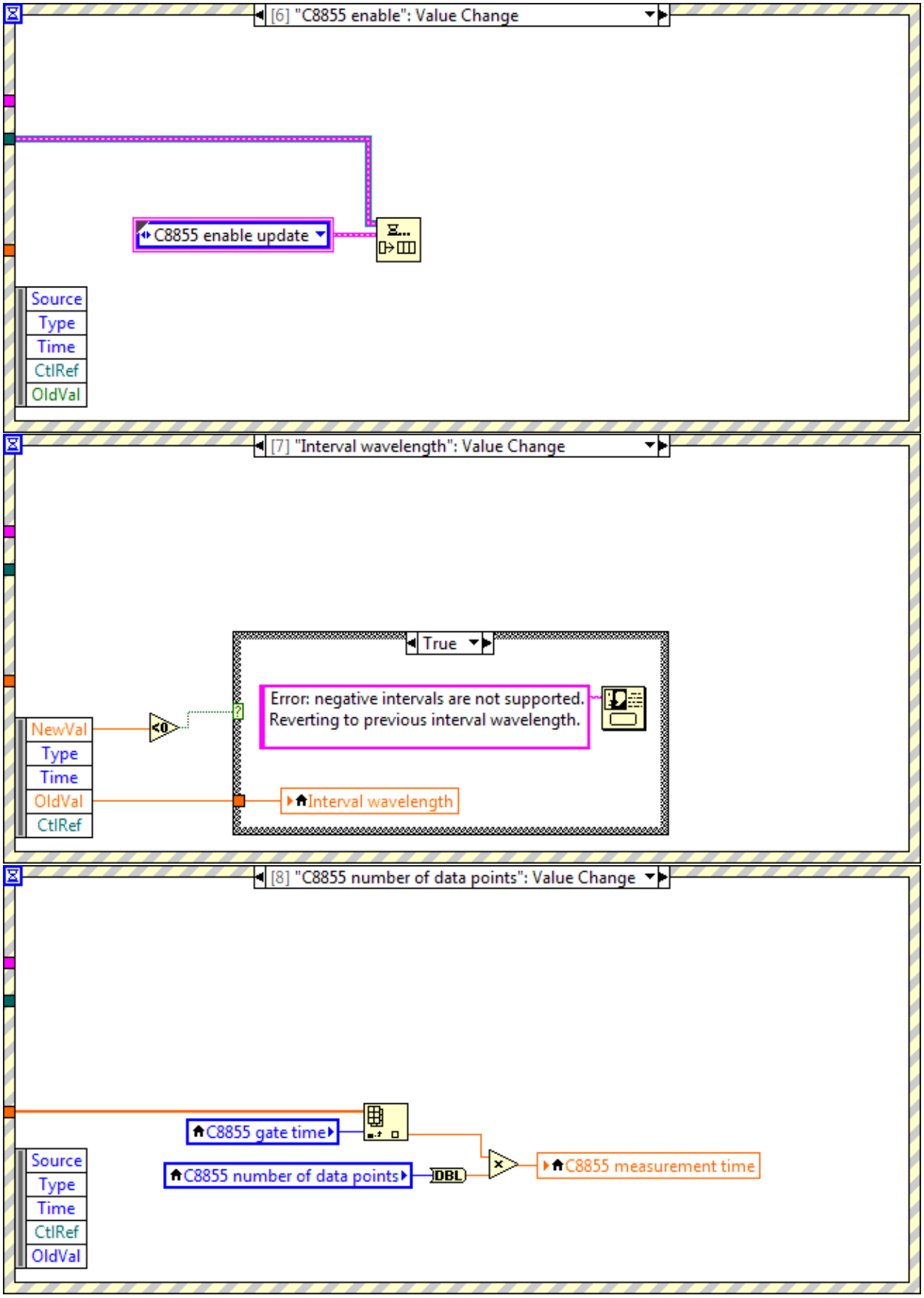
[6] "C8855 enable": Value Change
C8855 enable update
Source
Type
Time
CtlRef
OldVal
[7] "Interval wavelength": Value Change
True
Error: negative intervals are not supported.
Reverting to previous interval wavelength.
NewVal
Type
Time
OldVal
CtlRef
<0
Interval wavelength
[8] "C8855 number of data points": Value Change
C8855 gate time
C8855 number of data points
DBL
C8855 measurement time
Source
Type
Time
CtlRef
OldVal

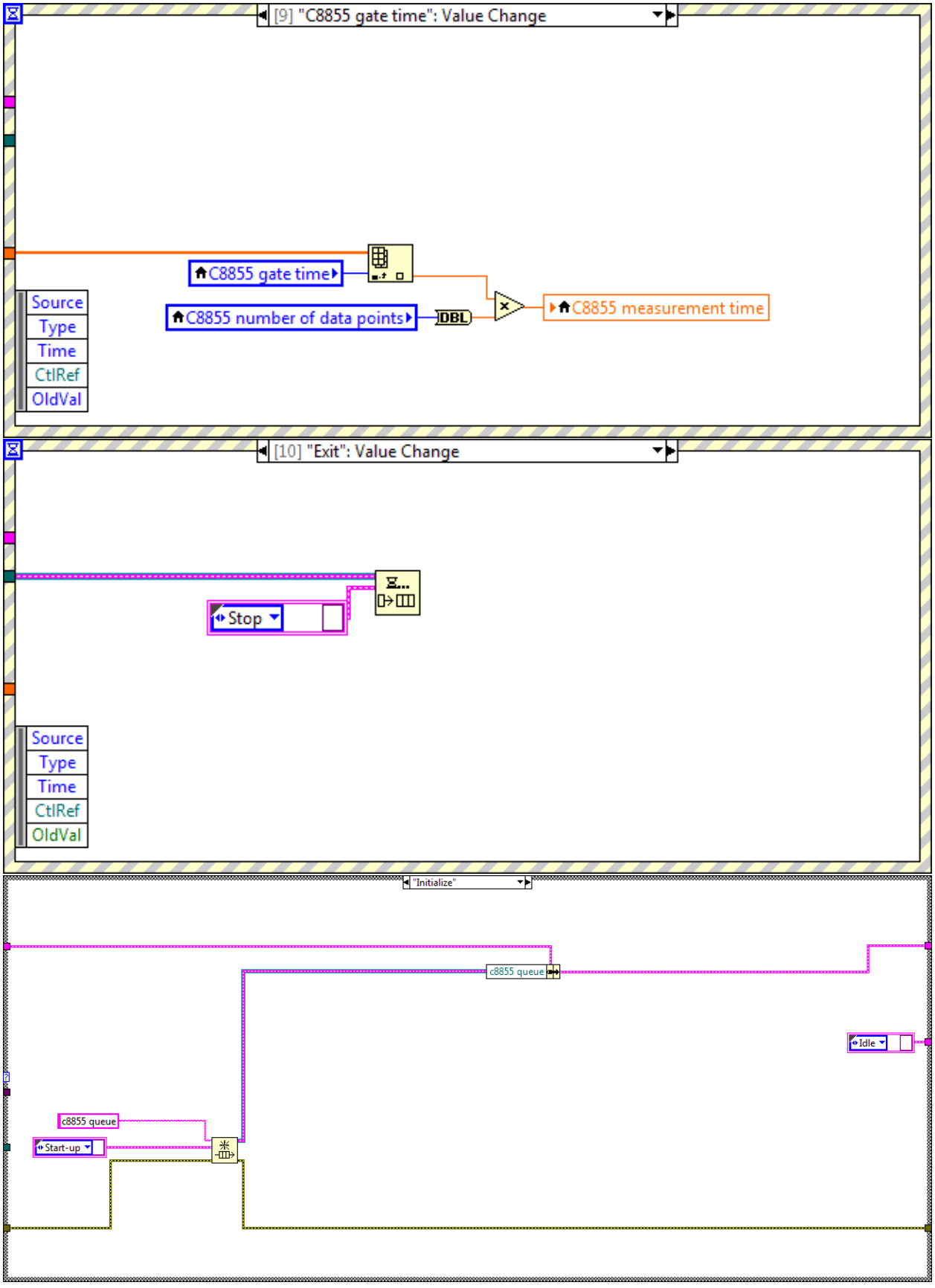
[9] "C8855 gate time": Value Change
C8855 gate time
C8855 number of data points
DBL
C8855 measurement time
Source
Type
Time
CtlRef
OldVal
[10] "Exit": Value Change
Stop
Source
Type
Time
CtlRef
OldVal
"Initialize"
c8855 queue
Idle
c8855 queue
Start-up

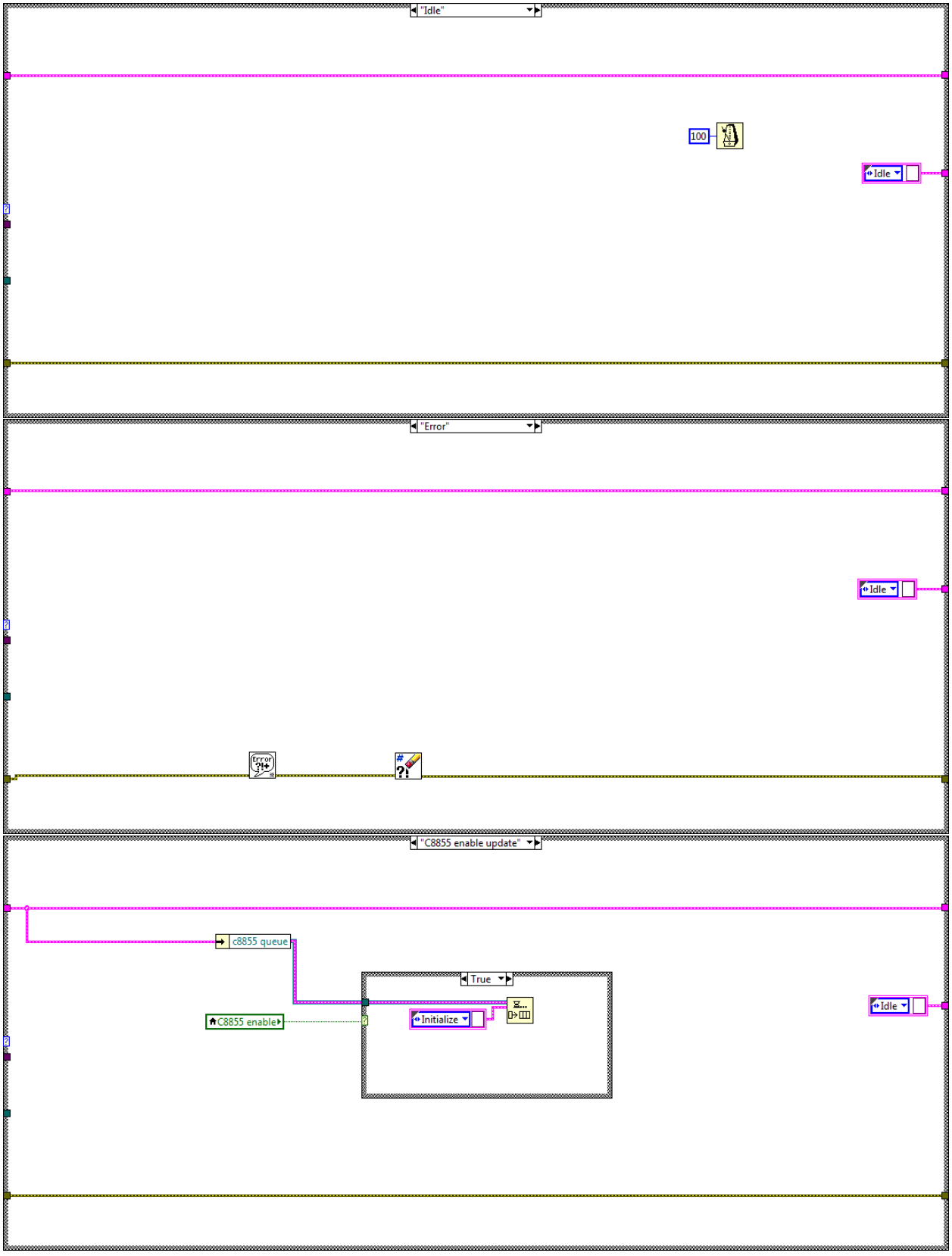
"Idle"
100
Idle
"Error"
Idle
Error
"C8855 enable update"
c8855 queue
True
C8855 enable
Initialize
Idle

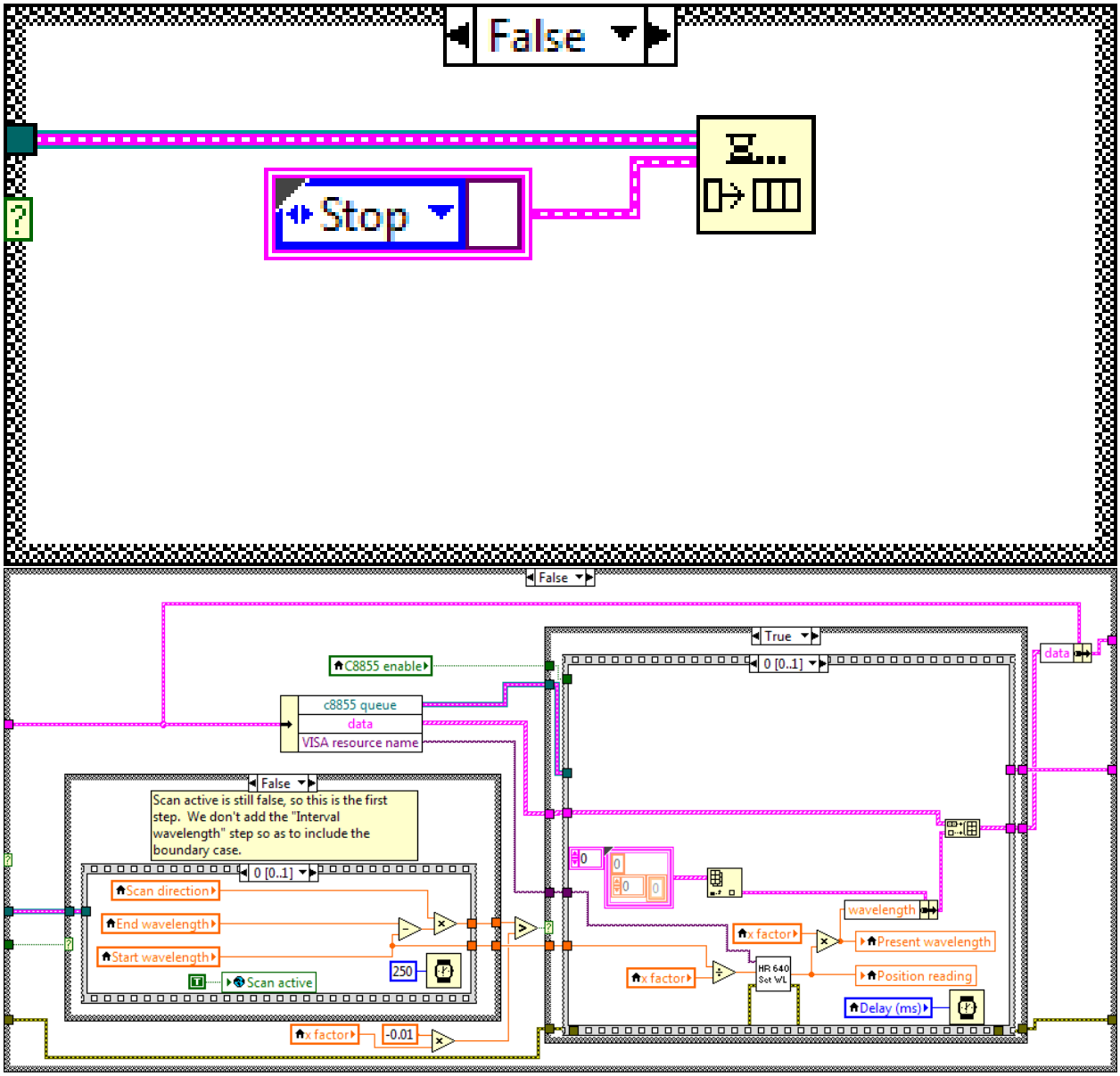
False
Stop
False
C8855 enable
c8855 queue
data
VISA resource name
False
Scan active is still false, so this is the first step. We don't add the "Interval wavelength" step so as to include the boundary case.
0 [0..1]
Scan direction
End wavelength
Start wavelength
Scan active
250
x factor
-0.01
True
0 [0..1]
data
wavelength
x factor
Present wavelength
x factor
HR 640 Set WL
Position reading
Delay (ms)

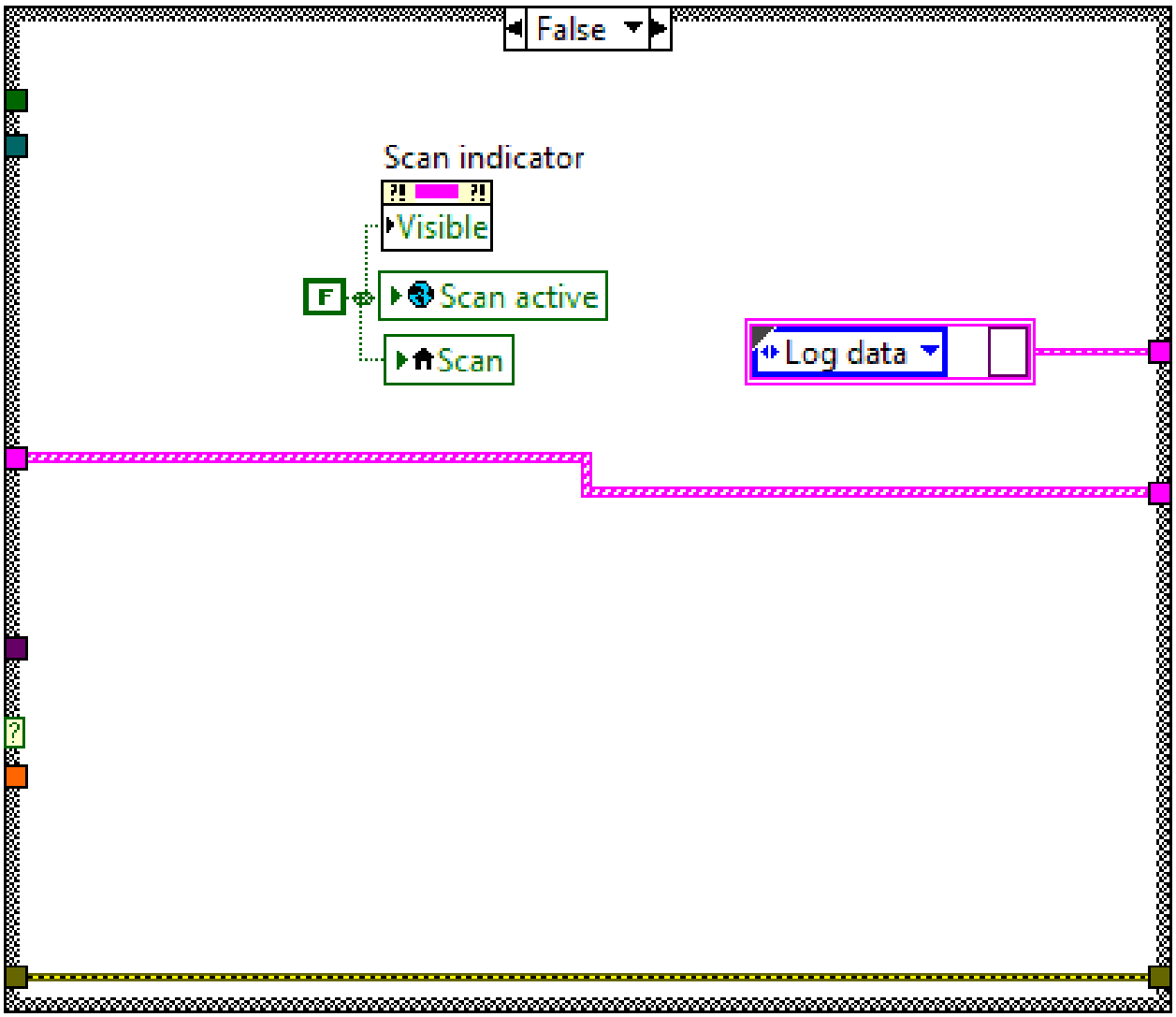
False
Scan indicator
Visible
F
Scan active
Scan
Log data

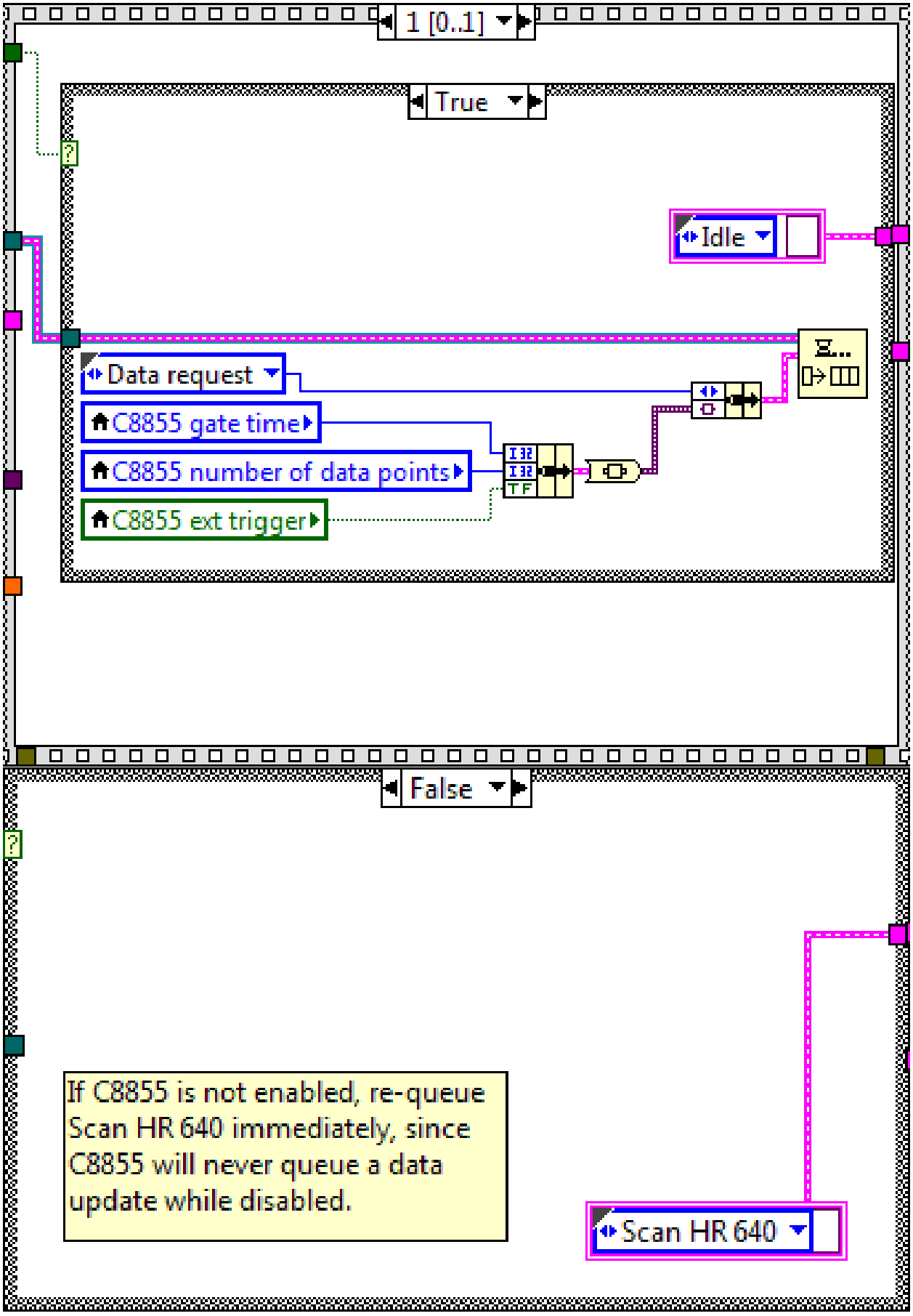
1 [0..1]
True
Idle
Data request
C8855 gate time
C8855 number of data points
C8855 ext trigger
False
If C8855 is not enabled, re-queue Scan HR 640 immediately, since C8855 will never queue a data update while disabled.
Scan HR 640

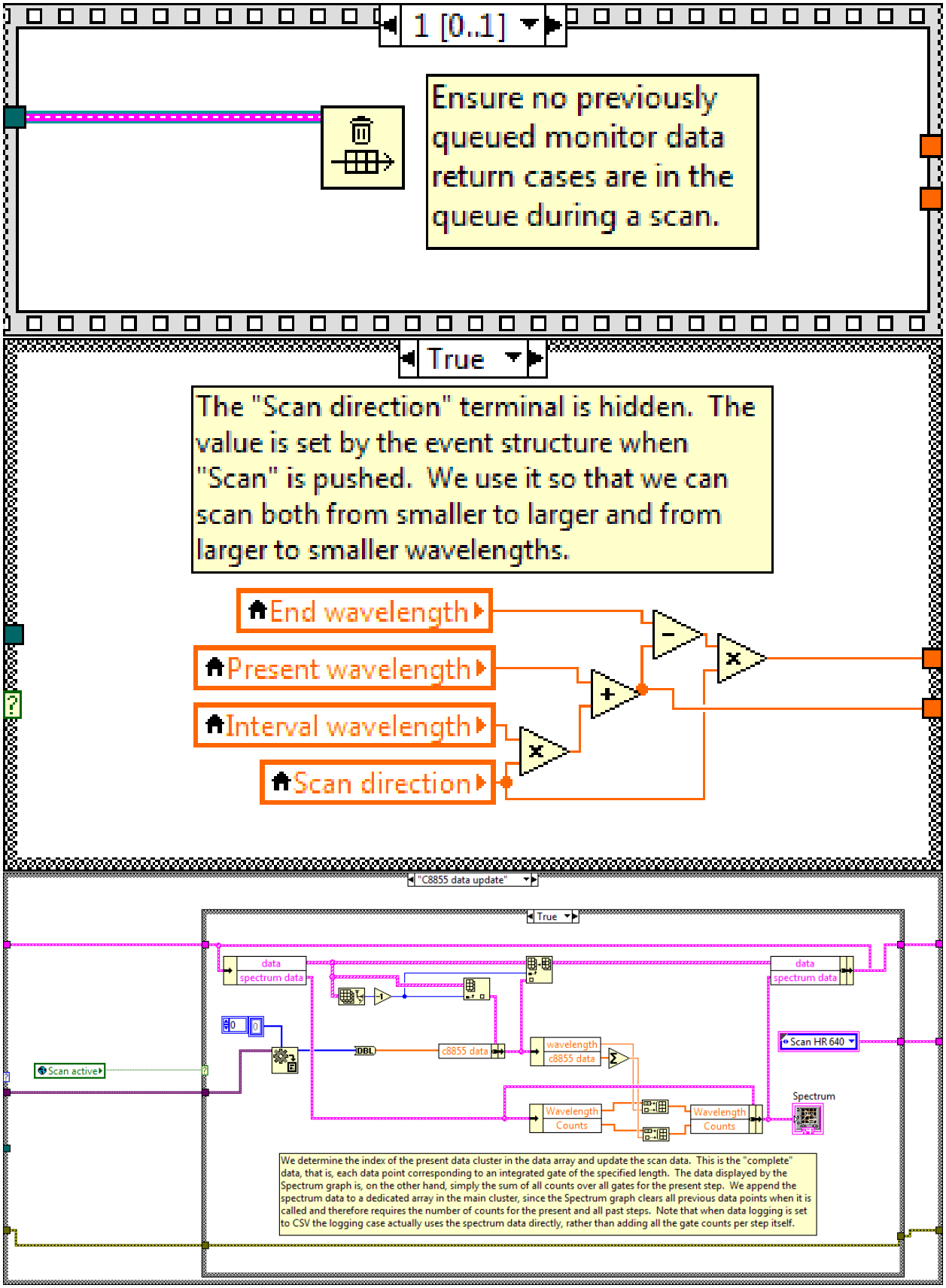
1 [0..1]
Ensure no previously queued monitor data return cases are in the queue during a scan.
True
The "Scan direction" terminal is hidden. The value is set by the event structure when "Scan" is pushed. We use it so that we can scan both from smaller to larger and from larger to smaller wavelengths.
End wavelength
Present wavelength
Interval wavelength
Scan direction
"C8855 data update"
True
data
spectrum data
Scan active
DBL
c8855 data
wavelength
c8855 data
Wavelength
Counts
Scan HR 640
Spectrum
We determine the index of the present data cluster in the data array and update the scan data. This is the "complete" data, that is, each data point corresponding to an integrated gate of the specified length. The data displayed by the Spectrum graph is, on the other hand, simply the sum of all counts over all gates for the present step. We append the spectrum data to a dedicated array in the main cluster, since the Spectrum graph clears all previous data points when it is called and therefore requires the number of counts for the present and all past steps. Note that when data logging is set to CSV the logging case actually uses the spectrum data directly, rather than adding all the gate counts per step itself.

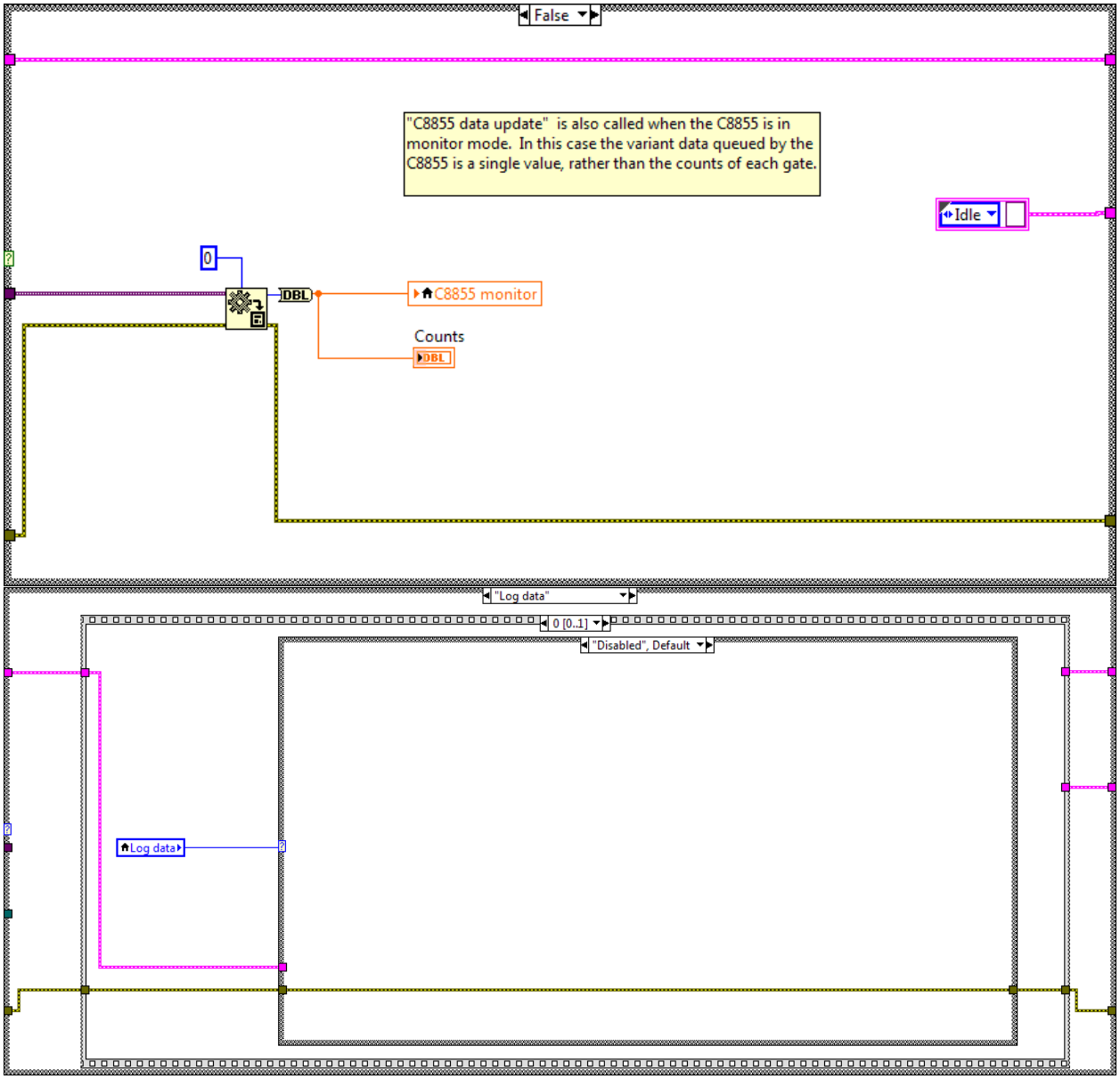
False
"C8855 data update" is also called when the C8855 is in monitor mode. In this case the variant data queued by the C8855 is a single value, rather than the counts of each gate.
Idle
0
DBL
C8855 monitor
Counts
DBL
"Log data"
0 [0..1]
"Disabled", Default
Log data

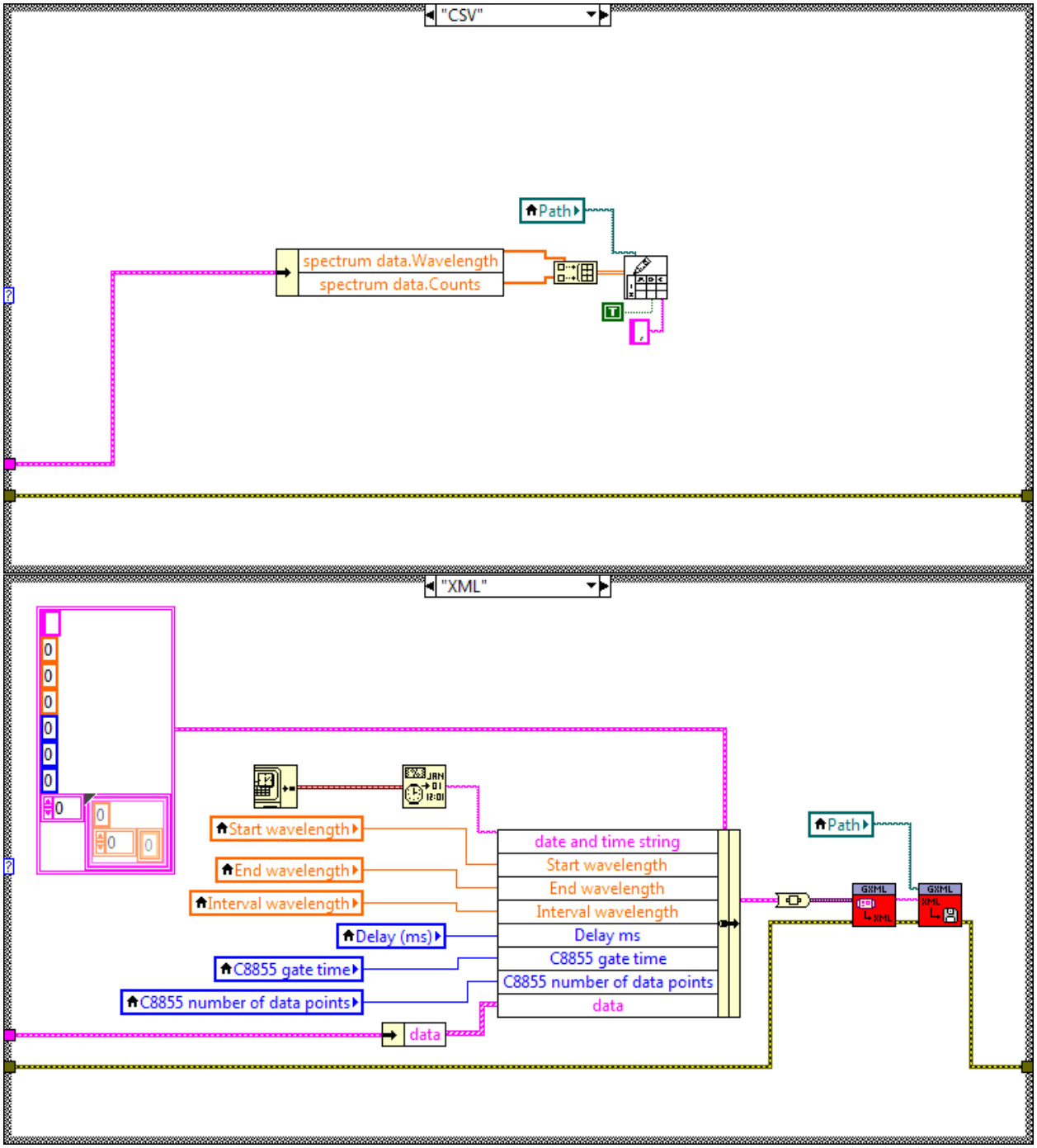
"CSV"
Path
spectrum data.Wavelength
spectrum data.Counts
"XML"
Start wavelength
End wavelength
Interval wavelength
Delay (ms)
C8855 gate time
C8855 number of data points
data
date and time string
Start wavelength
End wavelength
Interval wavelength
Delay ms
C8855 gate time
C8855 number of data points
data
Path

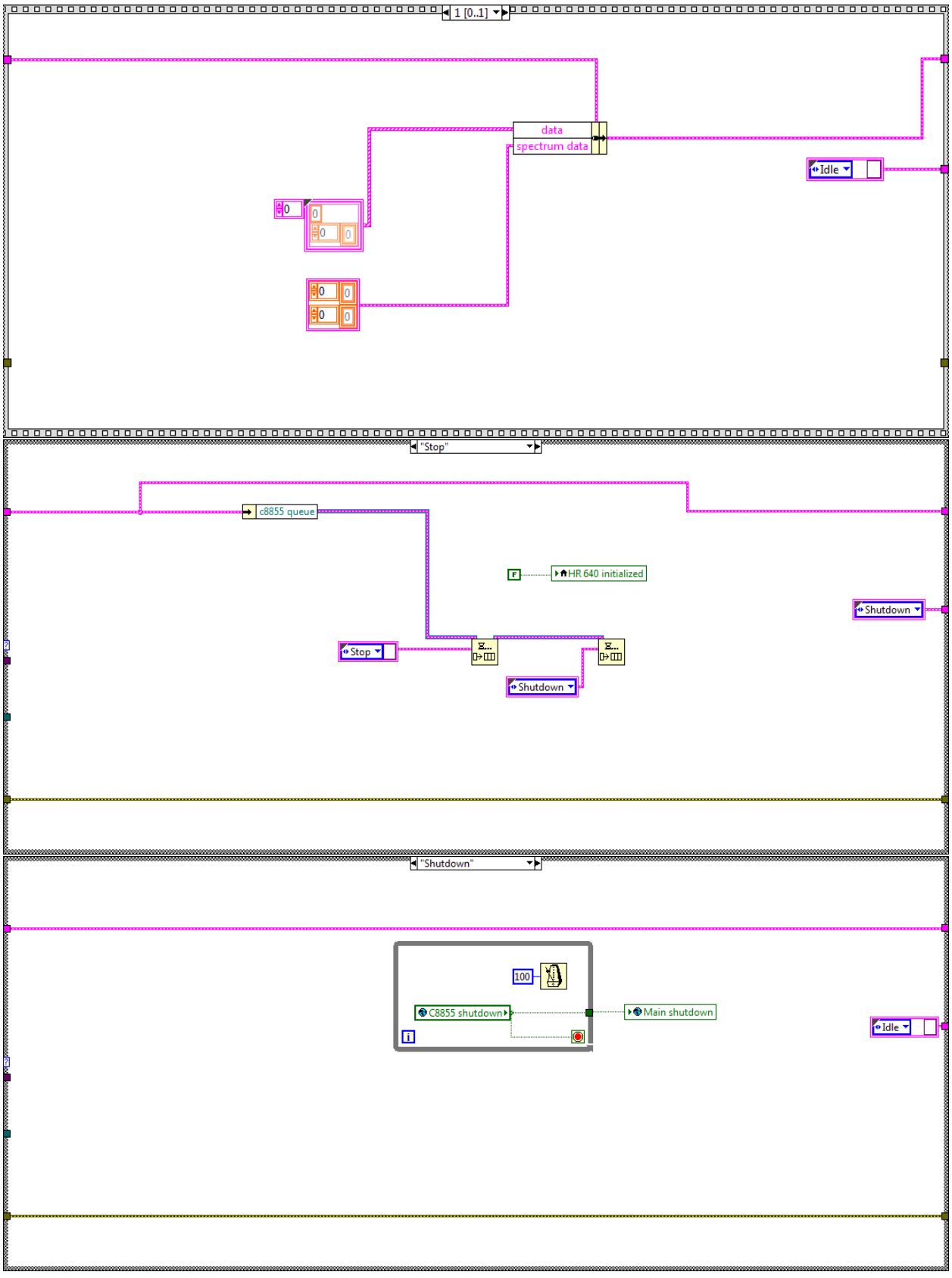
1 [0..1]
data
spectrum data
Idle
"Stop"
c8855 queue
HR 640 initialized
Shutdown
Stop
Shutdown
"Shutdown"
100
C8855 shutdown
Main shutdown
Idle

Bibliography

[1] G. Liu. *Spectroscopic Properties of Rare Earths in Optical Materials*. Springer Series in Materials Science. Springer, 2005.

[2] G. P. Flinn, K. W. Jang, J. Ganem, M. L. Jones, R. S. Meltzer, and R. M. Macfarlane. Anomalous optical dephasing in crystalline Y_2O_3:Eu^{3+}. *Journal of Luminescence*, 58(1):374 – 379, 1994.

[3] W. V. Smith and P. P. Sorokin. *The Laser*. McGraw-Hill Book Company, 1966.

[4] F. J. Duarte and R. O. James. Tunable solid-state lasers incorporating dye-doped, polymer-nanoparticle gain media. *Optical Letters*, 28(21):2088–2090, November 2003.

[5] J. K. Choi. *Laser spectroscopy of Eu centres in MBE grown CaF_2:Eu-CdF_2 superlattices and CaF_2:Eu thin films*. PhD thesis, University of Canterbury, 2009.

[6] F. Wang, X. Fan, D. Pi, and M. Wang. Synthesis and luminescence behavior of Eu^{3+}-doped CaF_2 nanoparticles. *Solid State Communications*, 133(12):775 – 779, 2005.

[7] C. Pandurangappa, B. N. Lakshminarasappa, and B. M. Nagabhushana. Synthesis and optical studies of gamma irradiated Eu doped nanocrystalline CaF_2. *Journal of Alloys and Compounds*, 509(29):7671 – 7673, 2011.

[8] M. Secu, C. E. Secu, S. Polosan, G. Aldica, and C. Ghica. Crystallization and spectroscopic properties of Eu-doped CaF_2 nanocrystals in transparent oxyfluoride glass-ceramics. *Journal of Non-Crystalline Solids*, 355(37–42):1869 – 1872, 2009.

[9] Gu. Wang, Q. Peng, and Y. Li. Upconversion luminescence of monodisperse CaF_2:Yb^{3+}/Er^{3+} nanocrystals. *Journal of the American Chemical Society*, 131(40):14200–14201, 2009.

[10] B. M. Tissue. Synthesis and luminescence of lanthanide ions in nanoscale insulating hosts. *Chemistry of Materials*, 10(10):2837–2845, September 1998.

[11] Y. Zhang, Q. Zhao, B. Shao, W. Lu, X. Dong, and H. You. Facile hydrothermal synthesis and luminescent properties of Eu-doped CaF_2-YF_3 alkaline-earth ternary fluoride microspheres. *RSC Adv.*, 4:35750–35756, 2014.

[12] Y. Jiang, P. Zhang, T. Wei, J. Fan, B. Jiang, X. Mao, and L. Zhang. Europium doped transparent glass ceramics containing CaF_2 micron-sized crystals: structural and optical characterization. *RSC Adv.*, 6:55366–55373, 2016.

[13] R. N. Bhargava. Doped nanocrystalline materials - physics and applications. *Journal of Luminescence*, 70:85–94, 1996.

[14] K. Hanaoka, K. Kikuchi, S. Kobayashi, and T. Nagano. Time-resolved long-lived luminescence imaging method employing luminescent lanthanide probes with a new microscopy system. *Americal Chemical Society*, 129(44):13502–13509, October 2007.

[15] X. Chen, Y. Liu, and D. Tu. *Lanthanide-Doped Luminescent Nanomaterials*. Springer, 2014.

[16] H. B. Beverloo, A. Van Schadewijk, S. van Gelderen-Boele, and H. J. Tanke. Inorganic phosphors and new luminescent labels for immunocytochemistry and time-resolved microscopy. *Cytometry*, 11(7):784–792, 1990.

[17] E. Beaurepaire, V. Buissette, M. P. Sauviat, D. Giaume, K. Lahlil, A. Mercuri, D. Casanova, A. Huignard, J. L. Martin, T. Gacoin, J. P. Boilot, and A. Alexandrou. Functionalized fluorescent oxide nanoparticles: Artificial toxins for sodium channel targeting and imaging at the single-molecule level. *Nano Letters*, 4(11):2079–2083, 2004.

[18] S. R. Lide. *CRC Handbook of Chemistry and Physics*. CRC Press, 85$^{\text{th}}$ edition, June 2004.

[19] G. W. Rubloff. Far-ultraviolet reflectance spectra and the electronic structure of ionic crystals. *Physical Review B*, 5:662–685, January 1972.

[20] Calcium fluoride (CaF_2). `http://www.crystran.co.uk/optical-materials/calcium-fluoride-caf2`. Accessed: 6th July, 2016.

[21] P. Denham, G. Field, P. Morse, and G. Wilkinson. Optical and dielectric properties and lattice dynamics of some fluorite structure ionic crystals. *Proceedings of the Royal Society of London, A. Mathematical and Physical Sciences*, 317(1528):55–77, 1970.

[22] P. S. Senanayake. *Two-Colour Excitation of Impurity Trapped Excitons in Wide Bandgap Insulators*. PhD thesis, University of Canterbury, October 2013.

[23] J. Corish, C. R. A. Catlow, P. W. M. Jacobs, and S. H. Ong. Defect aggregation in anion-excess fluorites. dopant monomers and dimers. *Phys. Rev. B*, 25:6425–6438, May 1982.

[24] K. M. Cirillo-Penn and J. C. Wright. Identification of defect structures in Eu^{3+}:CaF_2 by site selective spectroscopy of relaxation dynamics. *Journal of Luminescence*, 48:505 – 508, 1991.

[25] S. P. Jamison, R. J. Reeves, P. P. Pavlichuk, and G. D. Jones. Sharp resonance modes of cubic symmetry rare-earth ions in CaF_2-type crystals. *Journal of Luminescence*, 83–84:429 – 434, 1999.

[26] D. R. Tallant and J. C. Wright. Selective laser excitation of charge compensated sites in CaF_2:Er^{3+}. *J. Chem. Phys.*, 65(5):2074, 1982.

[27] M. Weissbluth. *Atoms and Molecules*. Academic Press (London), 1978.

[28] B. G. Wybourne. *Spectroscopic Properties of Rare Earths*. Interscience Publishers, 1965.

[29] B. R. Judd. *Operator Techniques in Atomic Spectroscopy*. McGraw-Hill Book Company, New York, 1963.

[30] E. U. Condon and G. H. Shortley. *The Theory of Atomic Spectra*. Cambridge University Press, Cambrdige, 1935.

[31] M. Rotenberg, R. Bivins, N. Metropolis, and J. K. Wooten Jr. *The 3-j and 6-j Symbols*. Technology Press, 1959.

[32] C. W. Nielson and G. F. Koster. *Spectroscopic Coefficients for the p^N, d^N and f^N Configurations*. M.I.T. Press (Massachusetts), 1963.

[33] M. Mujaji. *Solid State Spectroscopy: Laser Selective Excitation of Holmium Ions in Crystalline Solids*. PhD thesis, University of Canterbury, 1992.

[34] D. E. McCumber and M. D. Sturge. Linewidth and temperature shift of the R lines in ruby. *Journal of Applied Physics*, 34(6):1682–1684, 1963.

[35] G. S. Ofelt. Intensities of crystal spectra of rare earth ions. *The Journal of Chemical Physics*, 37(3):511–520, 1962.

[36] J. E. Lowther. Spectroscopic transition probabilities of rare earth ions. *Journal of Physics C: Solid State Physics*, 7(23):4393, 1974.

[37] G. F. Koster, J. O. Dimmock, R. G. Wheeler, and H. Statz. *Properties of the Thirty-Two Point Groups*. MIT Press, Cambridge, Massachusetts, 1963.

[38] Z. Quan, D. Yang, P. Yang, X. Zhang, H. Lian, X. Liu, and J. Lin. Uniform colloidal alkaline earth metal fluoride nanocrystals: Nonhydrolytic synthesis and luminescence properties. *Inorganic Chemistry*, 47(20):9509–9517, 2008. PMID: 18817372.

[39] J. P. R. Wells. *Laser Spectroscopy of Alkaline Earth Fluoride Crystals Doped With Trivalent Samarium and Europium Ions*. PhD thesis, University of Canterbury, 1996.

[40] S. V. Gastev, J. K. Choi, and R. J. Reeves. Laser spectroscopy of Eu^{3+} cubic centers in the CaF_2 bulk single crystal. *Physics of the Solid State*, 51(1):44–49, 2009.

[41] L. Song, J. Gao, and R. Song. Synthesis and luminescent properties of oleic acid (oa)-modified CaF_2: Eu nanocrystals. *Journal of Luminescence*, 130(7):1179 – 1182, 2010.

[42] L. H. Slooff, A. van Blaaderen, A. Polman, G. A. Hebbink, S. I. Klink, F. C. J. M. Van Veggel, D. N. Reinhoudt, and J. W. Hofstraat. Rare-earth doped polymers for planar optical amplifiers. *Journal of Applied Physics*, 91(7):3955–3980, 2002.

[43] A. F. Kirby and F. S. Richardson. Detailed analysis of the optical absorption and emission spectra of Eu^{3+} in the trigonal (C_3) $Eu(DBM)_3.H_2O$ system. *The Journal of Physical Chemistry*, 87(14):2544–2556, 1983.